Geochemical Perspectives Letters

Pyrite records fluid evolution: sulfur sources controls on arsenic speciation and zonation

A.P. Deditius[1], X. Yao[1], F. Xia[1*], J. Brugger[2], Y. Xing[2,3], B.E. Etschmann[2], A. Suvorova[4], M.P. Roberts[4], C.M. Kewish[5]

https://doi.org/10.7185/geochemlet.2603

Abstract

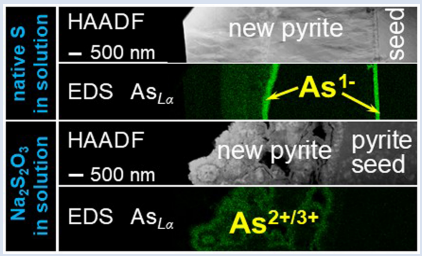

Zoning and speciation of arsenic (As) in pyrite are used to infer changes in the chemical composition of hydrothermal fluids and conditions of ore deposit formation. Yet, the processes controlling the distribution and oxidation state of As during pyrite formation are poorly understood. We report the results of experiments designed to test the capacity of pyrite to record changes in fluid composition under dynamic reaction conditions. When pyrite seeds were exposed alternately to As-bearing and As-free fluids, concentric As-rich (≤6.0 wt. % of As^{1-}) and As-free pyrite overgrowths formed when native S was used as the sulfur source. In contrast, a sodium thiosulfate source produced randomly oriented aggregates of concentrically zoned microparticulate (~1 μm) As-bearing pyrite (<1.5 wt. % of $As^{2+/3+}$), failing to record the changes of fluid composition. We demonstrate that by controlling $H_2S_{(aq)}$ availability, the source of sulfur affects the degree of pyrite supersaturation under conditions relevant to natural hydrothermal systems, which controls the nucleation rate, crystal growth, As uptake, As oxidation state, and consequently, the ability of pyrite to record individual fluid pulses. This sulfur source effect has significant implications for metal incorporation into pyrite and understanding of the formation of many ore deposits.

Received 18 February 2025 | Accepted 16 December 2025 | Published 22 January 2026

Introduction

The incorporation of arsenic and other trace elements into distinct zones during pyrite growth is one of the most prominent features that helps elucidate the evolution of fluid composition during ore deposition (Muntean *et al.*, 2011; Peterson and Mavrogenes, 2014; Morin *et al.*, 2017; Román *et al.*, 2019; Xing *et al.*, 2019). Commonly, pyrite growth zones are arranged in concentric As-rich and As-poor zones (Chouinard *et al.*, 2005) or as spongy porous aggregates of spheroidal particles deposited on barren pyrite (Deditius *et al.*, 2008; Genna and Gaboury, 2015). Lattice bound arsenic in pyrite occurs either as As^{1-} (Simon *et al.*, 1999; Manceau *et al.*, 2020) or $As^{2+/3+}$ (Deditius *et al.*, 2008; Qian *et al.*, 2013; Le Pape *et al.*, 2018), reflecting different incorporation mechanisms. Importantly, the concentrations and oxidation state of As in pyrite are some of the key parameters controlling the incorporation of Au into the mineral and its fate during the formation of gold deposits (*e.g.*, Reich *et al.*, 2005; Deditius *et al.*, 2014; Pokrovski *et al.*, 2021). Changes in the physicochemical parameters of the hydrothermal fluids, such as vigorous *vs.* gentle fluid boiling (Román *et al.*, 2019); the kinetics of crystal growth (Kusebauch *et al.*, 2018; Wu *et al.*, 2019); the type of As source (Qian *et al.*, 2013); and surface chemistry (Fleet and Mumin, 1997) were suggested to account for variable As concentrations, oxidation states, and zoning patterns in pyrite. Yet, the mechanisms controlling As scavenging by pyrite remain poorly understood.

Here, we show that changes in fluid composition affect the formation mechanism of zoned As pyrite overgrowing pyrite seeds (Table S-1). Different S sources, *i.e.* elemental S or thiosulphate ($Na_2S_2O_3{\cdot}5H_2O$), led to contrasting zoning textures and As oxidation states in the overgrowths after hydrothermal treatments that alternated between As-rich and As-free fluids at 200 °C (Table S-2). The aqueous solution compositions involved a mixture of oxidised (HSO_4^-, SO_4^{2-}) and reduced S species (HS^-, $H_2S_{(aq)}$) in the pyrite stability field, relevant for natural hydrothermal systems. Experimental details, analytical methods, and thermodynamic modelling results can be found in the Supplementary Information.

Results

Pyrite morphology, zoning, and composition. Addition of native S resulted in four concentric pyrite growth zones around the seeds (denoted as pyrite-S) (Fig. 1a–e), *i.e.* As-rich (Zones-1, -3) and

1. Sustainable Geochemistry and Mineral Sciences, School of Mathematics, Statistics, Chemistry and Physics, Murdoch University, Perth, WA 6150, Australia
2. School of Earth, Atmosphere and the Environment, Monash University, Clayton, VIC 3800, Australia
3. CSIRO Mineral Resources, Clayton, VIC 3168, Australia
4. Centre for Microscopy, Characterisation and Analysis, The University of Western Australia, Perth, WA 6009, Australia
5. Australian Synchrotron, Clayton, VIC 3168, Australia
* Corresponding author (Email: F.Xia@murdoch.edu.au)

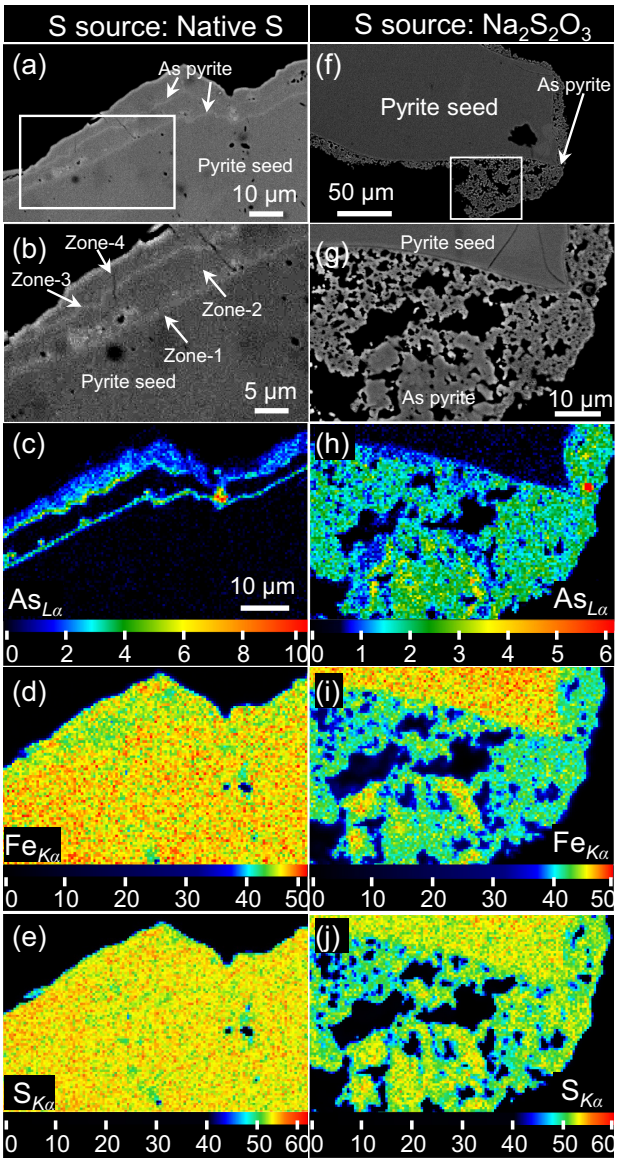

Figure 1 Backscattered electron images **(a, b, f, g)** and elemental mapping of As **(c, h)**, Fe **(d, i)**, and S **(e, j)** in newly formed pyrite. **(a–e)** Pyrite-S, **(f–j)** pyrite-SO. Note four zones of pyrite-S deposited on pyrite seed **(b)** and the sponge-like texture of pyrite-SO.

As depleted or As-free zones (Zones-2, -4). The alternating zones record the imposed variations in fluid composition. However, when native S was replaced with $Na_2S_2O_3{\cdot}5H_2O$, spongy aggregates (5–50 µm) of microparticulate As pyrite (denoted as pyrite-SO) formed instead (Fig. 1f–j); these textures do not reflect the chemical evolution of the system (Fig. 1c,h).

Electron probe microanalysis (EPMA) data show that the As concentrations in Zones-1 and -3 of pyrite-S vary broadly (0.02 to 6.02 wt. %), whereas pyrite-SO contains less As (<1.5 wt. %; Fig. S-1, Table S-3). High angle annular dark field scanning transmission electron microscopy (HAADF-STEM) observations and electron dispersive spectroscopy (EDS) analyses confirm the systematic textural and compositional changes across the four zones in pyrite-S (Figs. 2a,b, S-1 and S-2). Zones-1 and -3 are 200–300 nm thick and contain ≤5.8 wt. % and ≤4.7 wt. % As, respectively; Zones-2 and -4 are 3–5 µm thick and contain As (0.1 and 0.8 wt. %, respectively) near the contact with Zones-1 and -3 (Fig. 2b). Trails of pores occur along the contact between the pyrite seed and Zone-1; between Zones-2 and -3; and within Zone-4 (Fig. 2c–e). High resolution (HR) TEM and electron backscattered diffraction (EBSD) data show that, except for a few spherical misoriented domains (<500 nm) of As-bearing pyrite-S located near the contact between the seed and Zone-1, the lattice orientation of the zoned overgrowth aligns with that of the pyrite seed (Figs. S-3a, b, S-4a). This indicates the predominance of epitaxial growth. The Fast Fourier transformation (FFT) diffraction pattern from the Zone-1 HRTEM image documented rare realgar nanodomains ($d = 3.05$ Å) (Fig. S-5) in quantities below the detection limit of XRD (<0.1 wt. %) (Fig. S-6a).

Pyrite-SO is the only phase detected in the $Na_2S_2O_3{\cdot}5H_2O$ experiments (Fig. S-6b). It comprises concentrically zoned particles, randomly oriented and assembled into aggregates (Figs. 2f,g, S-3c,d, and S-4b). Porosity formed along the contacts between the 50–200 nm thick alternating zones of As-rich and As-poor pyrite (Fig. 2f). Some particles contain oval shaped As-rich (1.1–1.5 wt. %) cores, ~300 nm in diameter, followed by subhedral As depleted zones (0.2–0.7 wt. %), and by a third As enriched zone (~1.4 wt. %) (Fig. 2g). In some particles, a subhedral As depleted core formed first (Figs. S-7, S-8). In pyrite-SO, random As zoning reflects local fluid variations, whereas in pyrite-S the ordered four zone pattern records changes in bulk fluid composition (Figs. 1, 2).

Sulfur source affects arsenic incorporation in pyrite. Pyrite-S compositions plot along the As-S join, indicating the substitution of anionic As^{1-} for S; *i.e.* As substitutes as $[As_2]^{2-}$ for the $[S_2]^{2-}$ dimer (Manceau *et al.*, 2020) (Fig. 3a). In contrast, pyrite-SO compositions form a trend parallel to the Fe-S join towards the As corner of the ternary diagram, indicating cationic $As^{2+/3+}$ substitution for Fe^{2+} (Deditius *et al.*, 2008). These indirect EPMA and EDS results are corroborated by the X-ray absorption near edge structure (XANES) analyses (Fig. 3b,c).

Reaction conditions based on equilibrium thermodynamics. We used activity-activity diagrams to examine As and S speciation in fluids during pyrite formation (Fig. S-9), and aliquot-type thermodynamic modelling to predict reaction paths and mineral compositions resulting from progressive reactions with the two sulfur sources (native S or $Na_2S_2O_3$). These equilibrium models serve as a reference for discussing potential kinetic effects. The sulfur speciation in both systems was buffered near the bisulfide-sulfate boundary, at different bisulfide/sulfate ratios:

$$4S_{(s)} + 4H_2O = 2H^+ + 3H_2S_{(aq)} + SO_4^{2-}\ (3:1\ \text{bisulfide to sulfate}) \quad \text{Eq. 1}$$

$$S_2O_3^{2-} + H_2O = H_2S_{(aq)} + SO_4^{2-}\ (1:1\ \text{bisulfide to sulfate}) \quad \text{Eq. 2}$$

$As(OH)_{3(aq)}$ is the predominant species for As at the pH (~2–6) and redox conditions of the experiments, as it is in most hydrothermal fluids (James-Smith *et al.*, 2010; Testemale *et al.*, 2011). Note that arsenopyrite and realgar are predicted to form in $H_2S_{(aq)}$-rich, reduced ($aH_{2(aq)} > 10^{-10}$) fluids (Fig. S-9a). In our experiments, $H_2S_{(aq)}$ concentrations increase rapidly during sulfur dissolution (Fig. 4a,b), and hence the model predictions are consistent with the presence of small amounts of realgar in pyrite-S (Fig. S-5).

Pyrite is highly supersaturated in the initial solutions with a saturation index (SI) of ~8 for both sulfur sources (Fig. S-10). This SI increases to ~10 in the $Na_2S_2O_3{\cdot}5H_2O$ experiments; but decreases gradually towards ~6 in the S experiments (Fig. S-10). The predicted pH (neutral pH is 5.64 at 200 °C, P_{sat}) is slightly acidic (4.5–5) in the $Na_2S_2O_3{\cdot}5H_2O$ experiments (Fig. 4c), and

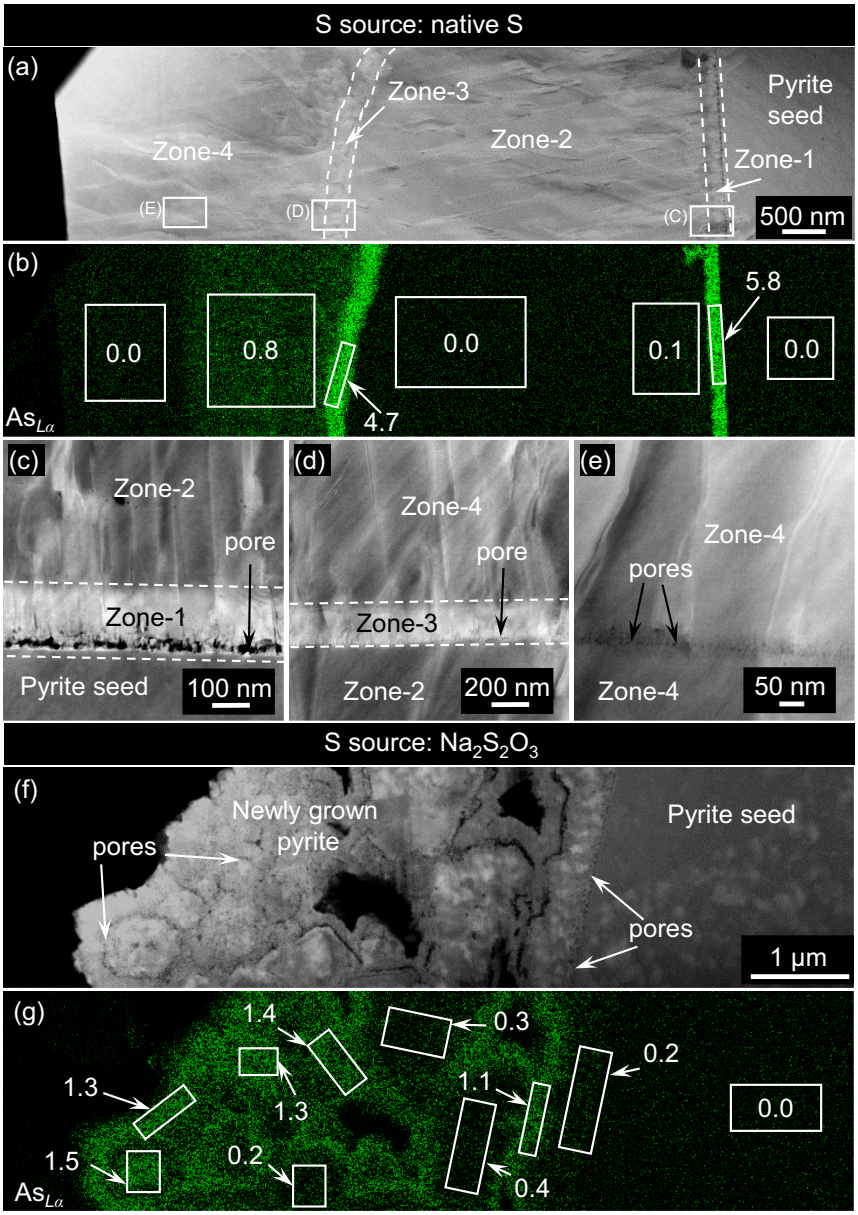

Figure 2 Summary of pyrite textures observed at higher resolution (HAADF-STEM) with corresponding TEM-EDS elemental maps of As. **(a, b)** Alternating As-in (Zones-1, -3) and As-out (Zones-2, -4) zones deposited on pyrite seed. **(b)** The rectangles and the values represent the areas of analysis and the concentration of As (in wt. %). **(c–e)** Porous pyrite formed between the seed and between the zones. **(f, g)** Aggregates of As zoned microcrystalline pyrite-SO. Note the porosity between the pyrite seed and the product and between the As-rich and As-poor zones of pyrite. **(a, b)** Pyrite-S; **(f, g)** pyrite-SO.

rapidly evolves towards more acidic (~3.2) conditions in the S experiments (Fig. 4d). The redox conditions in both experiments remain buffered close to the sulfate-bisulfide equilibrium (Fig. S-9b). The modelling predicts maximum As concentrations of 1000 ppm in pyrite-S and pyrite-SO, lower than the maxima measured in pyrite-S (6.0 wt. %) and pyrite-SO (1.5 wt. %). The predicted As partitioning coefficients between the mineral and fluid decrease by several orders of magnitude in the early stages of the reaction (Fig. 4e,f).

Discussion

Chemical zoning in minerals forms due to changes in fluid composition, temperature, and pressure (Shore and Fowler, 1996), kinetic factors, and/or self organisation (*e.g.*, Rakovan and Reeder, 1996). The alternating As-rich and As-free/poor zones in pyrite-S reflect the pulses of fluids with different compositions, but this record is absent in pyrite-SO (Figs. 1, 2).

The differences between pyrite-S and pyrite-SO are related to the S source, and its effect on the (super-)saturation state of pyrite. First, native S (<1 g/100 mL) is far less soluble than $Na_2S_2O_3{\cdot}5H_2O$ (73 g/100 mL). Second, the progressive disproportionation of thiosulfate (Eq. 2) increases the pyrite supersaturation level, whereas the disproportionation of sulfur (Eq. 1; Liu *et al.*, 2021) is predicted to decrease supersaturation (Fig. S-10). This is mainly because during pyrite precipitation (Fig. S-9), the same amounts of total S added result in a pH increase when using $Na_2S_2O_3{\cdot}5H_2O$, whereas native S causes a rapid pH decrease. This promotes fast nucleation of pyrite-SO and kinetically driven precipitation of spongy aggregates (Figs. 1f–j, 2f,g,

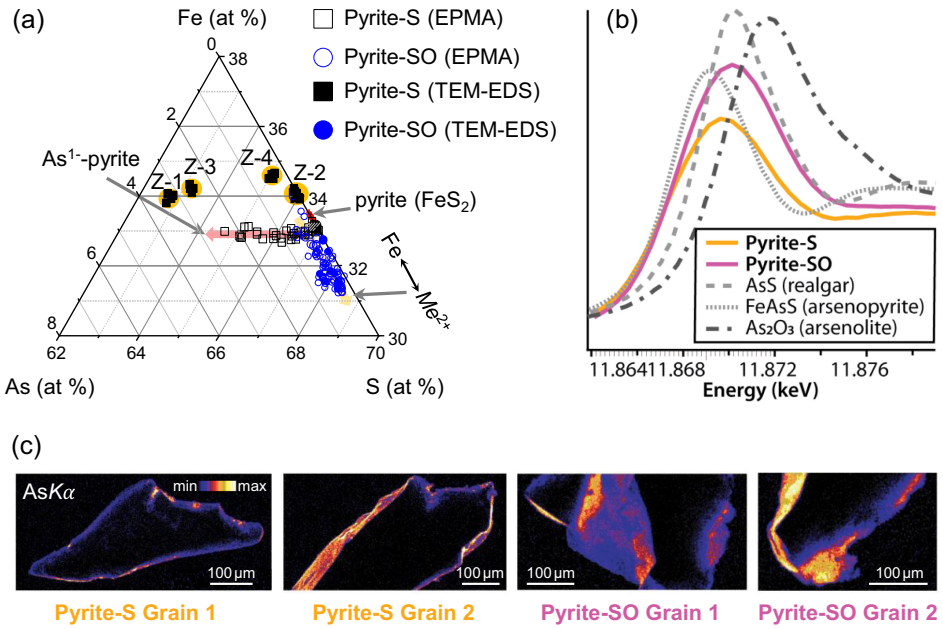

Figure 3 **(a)** Chemical composition of pyrite plotted in the As-Fe-S ternary. Filled symbols indicate the TEM-EDS analyses of Zones-1 to Zone-4 (Z-1 to Z-4). The coloured arrows indicate the trends associated with the substitution of (i) As for S (red), and (ii) Me^{2+} for Fe (yellow). Red cross; starting pyrite. **(b)** XANES spectra obtained on grains in **(c)**. **(c)** XFM maps showing the distribution of As in Pyrite-S (two grains, total 148 kpixel, with ~9000 As-rich) and Pyrite-SO (two grains, total 240 kpixel, including ~20,000 As-rich).

and S-9). In contrast, slower nucleation in the sulfur-bearing experiments resulted in epitaxial growth of pyrite S (Figs. S-3a, S-4a).

The XANES data indicate that As exists predominantly as As^{1-} in pyrite-S (Fig. 3b). Hence, the formation of pyrite-S from dissolved Fe, As and S under acidic conditions is described by:

$$Fe^{2+} + xAs(OH)_{3(aq)} + (2-x)H_2S_{(aq)} = FeS_{2-x}As_{x(s)} + (3x)H_2O + (1-2.5x)H_{2(aq)} + 2H^+ \quad \text{Eq. 3}$$

From the equilibrium constant K_3 of Equation 3, assuming a dilute solution, the value of the molal concentration of $As(OH)_{3(aq)}$ ($[As(OH)_{3(aq)}]$) is equal to the activity (a) of $As(OH)_{3(aq)}$, since $\gamma\ As(OH)_{3(aq)} \approx 1$, where γ is the activity coefficient. Similarly, for a small mole fraction (x) of the $FeAs_2$ component in arsenian pyrite, $\gamma FeAs_2 \approx 1$ according to the standard state based on Henry's law (Supplementary Information); hence, the values of the concentrations of $FeAs_2$ ($[FeAs_2]$, in mole fraction units) are identical to $aFeAs_2$. Using these assumptions, the partitioning coefficient for As between solid and solution is proportional to:

$$\log([FeAs_2]/[As(OH)_{3(aq)}]) \approx 1/x\{2\log K_3 + (5x-2)\log aH_{2(aq)} + 4pH + 2\log aFe^{2+} + x\log a(As(OH)_{3(aq)} + (4-2x)\log aH_2S_{(aq)}\} \quad \text{Eq. 4}$$

This indicates that the As partitioning coefficient is expected to change rapidly during precipitation, depending not only on the amounts of As in solution, but also on pH, redox, and the amounts of dissolved Fe and S. The thermodynamic model of Xing *et al.* (2019) and Equations 3, 4 assume As^{1-} substitution for S in pyrite, requiring a reduction of As^{3+} to As^{1-}. The rapid decrease in the As partitioning coefficient predicted by this thermodynamic model (Fig. 4) is primarily attributed to changes in pH and redox ($a\ H_{2(aq)}$) during the reaction.

In contrast, cationic $As^{2+/3+}$ substitutes for Fe^{2+} in pyrite-SO. Assuming As^{2+}:

$$(1-x)Fe^{2+} + xAs(OH)_{3(aq)} + 2H_2S_{(aq)} = (Fe_{1-x}As_x)S_{2(s)} + (3x)H_2O + (1-x/2)H_{2(aq)} + (2-2x)H^+ \quad \text{Eq. 5}$$

The stability constant K_5 for Equation 5 is:

$$\log([AsS_2]/[As(OH)_{3(aq)}]) \approx 1/x\{\log K_5 + (x/2-1)\log aH_{2(aq)} + (2-2x)pH + (1-x)\log aFe^{2+} + 2\log aH_2S_{(aq)}\} \quad \text{Eq. 6}$$

Compared to anionic As, the incorporation of cationic As is less sensitive to redox.

The thermodynamic modelling shows that the As contents in the pyrite-SO increase with pH when a small amount of S_2O_3 (<~0.15 mole S_{total}) is added (Fig. 4). For pyrite-S, adding similar amounts of native S results in a continuous decrease of As contents in pyrite, coinciding with pH decrease. Overall, the model results indicate that solution chemistry plays a critical role in controlling the precipitation and As content of arsenian pyrite.

Le Pape *et al.* (2017) reported that the polysulfide pathway of pyrite formation generates more oxidising conditions than when reacting FeS with $H_2S_{(aq)}$, facilitating the incorporation of $As^{2+/3+}$. However, incorporation of $As^{2+/3+}$ into pyrite-SO suggests that cationic As in pyrite may not only be related to a relatively higher oxidation state but also to the kinetics of pyrite formation; *i.e.* nucleation is the predominant process for pyrite-SO precipitation at high supersaturation levels, whereas growth is the predominant process for pyrite-S. Thermodynamic modelling suggests that the fluid redox differs only slightly between both experiments ($\Delta\log aH_{2(aq)} < 1$; Fig. 4c,d). The incorporation of $As^{2+/3+}$ introduces structural distortion, which is balanced by the formation of vacancies (Deditius *et al.*, 2008) and is favoured by rapid growth.

Implications for As geochemistry and the formation of ore deposits. The new experiments illustrate how arsenian pyrite

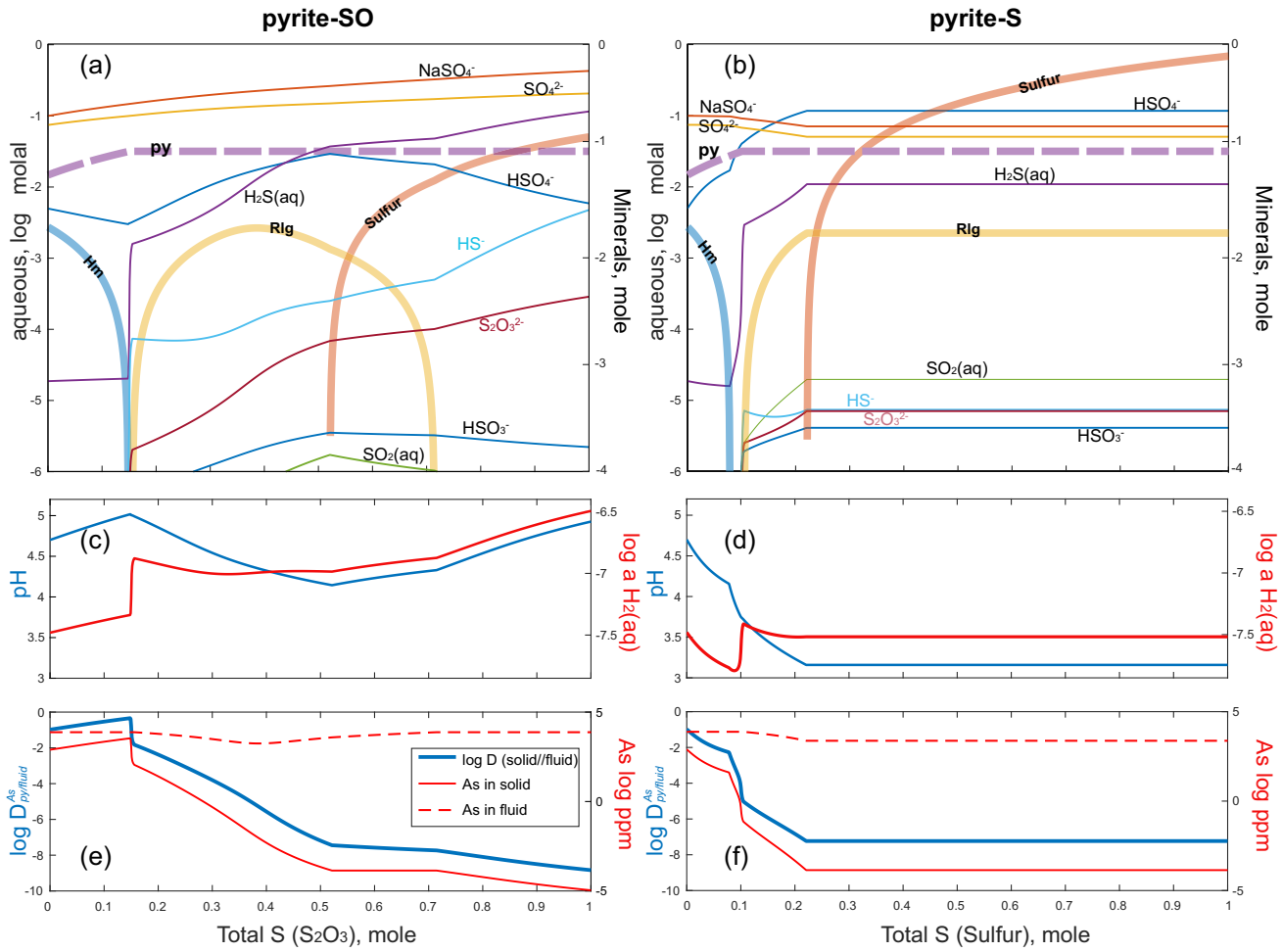

Figure 4 Model results of titrating different S sources as Na sulfite or native sulfur to precipitate arsenian pyrite. **(a, c, e)** The $Na_2S_2O_3$ system, and **(b, d, f)** the native sulfur system. Panels **(a, b)** show the amounts of mineral present (thick lines) and the dominant aqueous sulfur species (thin solid lines). Panels **(c, d)** show redox as *a* $H_{2(aq)}$ (right axes) and solution pH (left axes). Panels **(e, f)** display the variations in As concentrations and partitioning coefficients between pyrite and fluid; $D^{As}_{py/fluid}$ is the partitioning coefficient in ppm and is plotted on the left axis. Mineral abbreviations: py, pyrite; Hm, hematite; Rlg, realgar.

precipitation and associated dynamic changes in fluid composition (pH, redox, As and Fe contents) result in different As speciation (anionic *vs.* cationic As substitution) and variable product morphology arising from different mechanisms of pyrite growth (epitaxial *vs.* nucleation of randomly oriented particles) (Figs. 1–3). Thus, these results help explain the natural variability of pyrite textures in porphyry epithermal, volcanic-hosted massive sulfide (VMS), and Carlin-type ore deposits, as well as in hydrothermal vents. In these dynamic environments, zoned As pyrite forms during fluid boiling/phase separation and/or mixing of seawater or meteoric water with hydrothermal fluids, and/or rapid fluid-rock interactions commonly in the presence of pre-existing pyrite, as documented by changes in S isotopes (Reich *et al.*, 2013; Peterson and Mavrogenes, 2014; Franchini *et al.*, 2015; Román *et al.*, 2019; McLeish *et al.*, 2024; Schaarschmidt *et al.*, 2021; Holley *et al.*, 2024; Xiao *et al.*, 2025). Resulting pyrite textures exhibit a single type, or a mixture of euhedral oscillatory zoned grains (pyrite-S) associated with collomorphic overgrowths and/or aggregates of spongy pyrite (pyrite-SO) reflecting the change in the conditions of the hydrothermal systems.

A higher proportion of oxidised S species is expected during flash vapourisation of hydrothermal fluids at low pressures and/or extreme disproportionation of magmatic SO_2 (Reeves *et al.*, 2011; Peterson and Mavrogenes, 2014). The epitaxial growth of As-bearing pyrite-S resembles the structure of As pyrite in porphyry and epithermal gold deposits (Chouinard *et al.*, 2005; Deditius *et al.*, 2008; Peterson and Mavrogenes, 2014). There, pyrite records the transition from porphyry to epithermal conditions, through As, Au, and chalcophile element-rich rims overgrowing a (Co, Ni)-bearing euhedral porphyry pyrite core (Fig. 1) (Reich *et al.*, 2013; Peterson and Mavrogenes, 2014; Franchini *et al.*, 2015). Porosity aligned with the contact between the As-rich zones and As-free pyrite (Fig. 2) highlights the change in the fluid chemistry. A similar texture was interpreted to signify enrichment of chalcophile elements in arsenian pyrite during fluid boiling in hydrothermal systems (Román *et al.*, 2019). Importantly, the textural changes and porosity (Figs. 1, S-1) from As-rich to As-poor may be the only evidence of changing conditions during continuous growth of pyrite without disturbing the S isotopic signature (McLeish *et al.*, 2024).

The spherical morphology and randomly orientated pyrite-SO, often detached from the pyrite seed (Figs. S-7, S-8), resembles textures in Carlin-type gold deposits formed during mixing of meteoric water and hydrothermal fluids interacting with pre-existing pyrite traps (Muntean *et al.*, 2011; Holley *et al.*, 2024), or those in hydrothermal pyrite precipitated under far from equilibrium conditions of hydrothermal vents during the mixing of the hot fluids with seawater with decreasing $H_2S_{(aq)}$ concentrations (Gartman and Luther, 2013; McLeish *et al.*, 2024; Schaarschmidt *et al.*, 2021). The variable concentrations of As in pyrite-SO

resemble the internally heterogeneous nanoscale concentric As zonation of pyrite from Carlin-type gold deposits, stemming from the partial replacement of pre-existing As-rich zones and liberation of As into the fluid. This process explains the formation of the aggregates of randomly oriented nanoparticles on the sedimentary pyrite or detached from its surface (Holley *et al.*, 2024; Xiao *et al.*, 2025). Epitaxial growth of As pyrite on the pyrite core was explained by means of decoupled dissolution of the core and subsequent precipitation of the As pyrite rim (Xiao *et al.*, 2025).

In nature, most As pyrite contains anionic As substituting for S (Deditius *et al.*, 2014). Epitaxial overgrowth of pyrite by As pyrite (Fig. S-5) or recrystallised As pyrite hosts As^{1-}, while fast nucleation of spherical, randomly oriented pyrite sequesters cationic $As^{2+/3+}$. We find that the incorporation of anionic or cationic As into pyrite (Figs. 1–3) may depend on pyrite saturation levels. At high S concentrations (high supersaturation), pyrite incorporates cationic As, since no (or little) redox reaction is required (Eqs. 3–6; Figs. 1, 2 and 4).

In addition, the ppm-based As partitioning coefficient, $D^{As}_{py/fluid}$ (= [As (ppm) in pyrite/As (ppm) in fluid]) for pyrite-S (~100), is an order of magnitude higher than in pyrite-SO (~12), following the decreasing trend with increasing As concentration in the fluid (Figs. S-11, S-12) (Kusebauch *et al.*, 2018). This may stem from different mechanisms of incorporation of anionic *vs.* cationic As species; thermodynamically controlled (Eq. 2) growth of arsenian pyrite-S and nucleation of pyrite-SO. In nucleation controlled pyrite-SO, the As zoning does not reflect As-rich and As-free pulses, *i.e.* pyrite-SO does not preserve the history of successive fluid inputs (Holley *et al.*, 2024). Consequently, the incorporation of other metals, such as Au, Cu, Co, Ni, and Zn, which often coexist with As (Parnell *et al.*, 2018; Domingos *et al.*, 2023), may be limited, therefore affecting the capability of pyrite to record the composition of the hydrothermal fluid. These results provide important and first hand information on how mineral formation responds to changing fluid chemistry, with implications for a detailed understanding of ore deposit-forming processes.

Acknowledgements

The authors acknowledge funding from the Australian Research Council (DP170101893, DP220100500); the Australian Microscopy and Microanalysis Research Facility at the Centre for Microscopy, Characterisation and Analysis, The University of Western Australia; and The Australian Synchrotron, part of ANSTO, for access to the Powder Diffraction and X-ray Fluorescence Microscopy beamlines. XY acknowledges Murdoch University for a Strategic Scholarship. We are grateful to Gleb Pokrovski, Denis Fougerouse, Duncan McLeish, two anonymous reviewers, and editor Eric Oelkers for their insightful suggestions, which helped us to improve this manuscript.

Editor: Eric Oelkers

Additional Information

Supplementary Information accompanies this letter at https://www.geochemicalperspectivesletters.org/article2603.

Cite this letter as: Deditius, A.P., Yao, X., Xia, F., Brugger, J., Xing, Y., Etschmann, B.E., Suvorova, A., Roberts, M.P., Kewish, C.M. (2026) Pyrite records fluid evolution: sulfur sources controls on arsenic speciation and zonation. *Geochem. Persp. Let.* 38, 53–59. https://doi.org/10.7185/geochemlet.2603

References

Chouinard, A., Paquette, J., Williams-Jones, A.E. (2005) Crystallographic controls on trace-element incorporation in auriferous pyrite from the Pascua epithermal high-sulfidation deposit, Chile–Argentina. *The Canadian Mineralogist* 43, 951–963. https://doi.org/10.2113/gscanmin.43.3.951

Deditius, A.P., Utsunomiya, S., Renock, D., Ewing, R.C., Ramana, C.V., Becker, U., Kesler, S.E. (2008) A proposed new type of arsenian pyrite: Composition, nanostructure and geological significance. *Geochimica et Cosmochimica Acta* 72, 2919–2933. https://doi.org/10.1016/j.gca.2008.03.014

Deditius, A.P., Reich, M., Kesler, S.E., Utsunomiya, S., Chryssoulis, S.L., Walshe, J., Ewing, R.C. (2014) The coupled geochemistry of Au and As in pyrite from hydrothermal ore deposits. *Geochimica et Cosmochimica Acta* 140, 644–670. https://doi.org/10.1016/j.gca.2014.05.045

Domingos, J.M., Runge, E., Dreher, C., Chiu, T.-H., Shuster, J., Fischer, S., Kappler, A., Duda, J.-P., Xu, J., Mansor, M. (2023) Inferred pyrite growth via the particle attachment pathway in the presence of trace metals. *Geochemical Perspectives Letters* 26, 14–19. https://doi.org/10.7185/geochemlet.2318

Fleet, M.E., Mumin, A.H. (1997) Gold-bearing arsenian pyrite and marcasite and arsenopyrite from Carlin Trend gold deposits and laboratory synthesis. *American Mineralogist* 82, 182–193. https://doi.org/10.2138/am-1997-1-220

Franchini, M., McFarlane, C., Maydagán, L., Reich, M., Lentz, D.R., Meinert, L., Bouhier, V. (2015) Trace metals in pyrite and marcasite from the Agua Rica porphyry-high sulfidation epithermal deposit, Catamarca, Argentina: Textural features and metal zoning at the porphyry to epithermal transition. *Ore Geology Reviews* 66, 366–387. https://doi.org/10.1016/j.oregeorev.2014.10.022

Gartman, A., Luther III, G.W. (2013) Comparison of pyrite (FeS_2) synthesis mechanisms to reproduce natural FeS_2 nanoparticles found at hydrothermal vents. *Geochimica et Cosmochimica Acta* 120, 447–458. https://doi.org/10.1016/j.gca.2013.06.016

Genna, D., Gaboury, D. (2015) Deciphering the Hydrothermal Evolution of a VMS System by LA-ICP-MS Using Trace Elements in Pyrite: An Example from the Bracemac-McLeod Deposits, Abitibi, Canada, and Implications for Exploration. *Economic Geology* 110, 2087–2108. https://doi.org/10.2113/econgeo.110.8.2087

Holley, E.A., Jilly-Rehak, C., Fulton, A.A., Gorman, B. (2024) Trace Element Zonation in Carlin-Type Pyrite: Tracking Ore-Forming Processes at the Nanoscale. *Economic Geology* 119, 1139–1169. https://doi.org/10.5382/econgeo.5089

James-Smith, J., Cauzid, J., Testemale, D., Liu, W., Hazemann, J.-L., Proux, O., Etschmann, B., Philippot, P., Banks, D., Williams, P., Brugger, J. (2010) Arsenic speciation in fluid inclusions using micro-beam X-ray absorption spectroscopy. *American Mineralogist* 95, 921–932. https://doi.org/10.2138/am.2010.3411

Kusebauch, C., Oelze, M., Gleeson, S.A. (2018) Partitioning of arsenic between hydrothermal fluid and pyrite during experimental siderite replacement. *Chemical Geology* 500, 136–147. https://doi.org/10.1016/j.chemgeo.2018.09.027

Le Pape, P., Blanchard, M., Brest, J., Boulliard, J.-C., Ikogou, M., Stetten, L., Wang, S., Landrot, G., Morin, G. (2017) Arsenic Incorporation in Pyrite at Ambient Temperature at Both Tetrahedral S^{-I} and Octahedral Fe^{II} Sites: Evidence from EXAFS–DFT Analysis. *Environmental Science & Technology* 51, 150–158. https://doi.org/10.1021/acs.est.6b03502

Le Pape, P., Blanchard, M., Juhin, A., Rueff, J.-P., Ducher, M., Morin, G., Cabaret, D. (2018) Local environment of arsenic in sulfide minerals: insights from high-resolution X-ray spectroscopies, and first-principles calculations at the As K-edge. *Journal of Analytical Atomic Spectrometry* 33, 2070–2082. https://doi.org/10.1039/C8JA00272J

Liu, W., Spinks, S.C., Glenn, M., MacRae, C., Pearce, M.A. (2021) How carbonate dissolution facilitates sediment-hosted Zn-Pb mineralization. *Geology* 49, 1363–1368. https://doi.org/10.1130/G49056.1

Manceau, A., Merkulova, M., Mathon, O., Glatzel, P., Murdzek, M., Batanova, V., Simionovici, A., Steinmann, S.N., Paktunc, D. (2020) The Mode of

Incorporation of As(-I) and Se(-I) in Natural Pyrite Revisited. *ACS Earth and Space Chemistry* 4, 379–390. https://doi.org/10.1021/acsearthspacechem.9b00301

McLeish, D.F., Williams-Jones, A.E., Clark, J.R., Stern, R.A. (2024) Extreme shifts in pyrite isotope compositions reveal the path to bonanza gold. *Proceedings of the National Academy of Sciences* 121, e2402116121. https://doi.org/10.1073/pnas.2402116121

Morin, G., Noël, V., Menguy, N., Brest, J., Baptiste, B., Tharaud, M., Ona-Nguema, G., Ikogou, M., Viollier, E., Juillot, F. (2017) Nickel accelerates pyrite nucleation at ambient temperature. *Geochemical Perspectives Letters* 5, 6–11. https://doi.org/10.7185/geochemlet.1738

Muntean, J.L., Cline, J.S., Simon, A.C., Longo, A.A. (2011) Magmatic–hydrothermal origin of Nevada's Carlin-type gold deposits. *Nature Geoscience* 4, 122–127. https://doi.org/10.1038/ngeo1064

Parnel, J., Perez, M., Armstrong, J., Bullock, L., Feldmann, J., Boyce, A.J. (2018) Geochemistry and metallogeny of Neoproterozoic pyrite in oxic and anoxic sediments. *Geochemical Perspectives Letters* 7, 12–16. https://doi.org/10.7185/geochemlet.1812

Peterson, E.C., Mavrogenes, J.A. (2014) Linking high-grade gold mineralization to earthquake-induced fault-valve processes in the Porgera gold deposit, Papua New Guinea. *Geology* 42, 383–386. https://doi.org/10.1130/G35286.1

Pokrovski, G.S., Escoda, C., Blanchard, M., Testemale, D., Hazemann, J.-L., Guoy, S., Kokh, M.A., Boiron, M.-C., de Parseval, F., Aigouy, T., Menjot, L., de Parseval, P., Proux, O., Rovezzi, M., Béziat, D., Salvi, S., Kouzmanov, K., Bartsch, T., Pöttgen, R., Doert, T. (2021) An arsenic-driven pump for invisible gold in hydrothermal systems. *Geochemical Perspectives Letters* 17, 39–44. https://doi.org/10.7185/geochemlet.2112

Qian, G., Brugger, J., Testemale, D., Skinner, W., Pring, A. (2013) Formation of As(II)-pyrite during experimental replacement of magnetite under hydrothermal conditions. *Geochimica et Cosmochimica Acta* 100, 1–10. https://doi.org/10.1016/j.gca.2012.09.034

Rakovan, J., Reader, R.J. (1996) Intracrystalline rare earth element distributions in apatite: Surface structural influences on incorporation during growth. *Geochimica et Cosmochimica Acta* 60, 4435–4445. https://doi.org/10.1016/S0016-7037(96)00244-X

Reeves, E.P., Seewald, J.S., Saccocia, P., Bach, W., Craddock, P.R., Shanks, W.C., Sylva, S.P., Walsh, E., Pichler, T., Rosner, M. (2011) Geochemistry of hydrothermal fluids from the PACMANUS, Northeast Paul and Vienna Woods hydrothermal fields, Manus Basin, Papua New Guinea. *Geochimica et Cosmochimica Acta* 75, 1088–1123. https://doi.org/10.1016/j.gca.2010.11.008

Reich, M., Kesler, S.E., Utsunomiya, S., Palenik, C.S., Chryssoulis, S.L., Ewing, R.C. (2005) Solubility of gold in arsenian pyrite. *Geochimica et Cosmochimica Acta* 69, 2781–2796. https://doi.org/10.1016/j.gca.2005.01.011

Reich, M., Deditius, A., Chryssoulis, S., Li, J.-W., Ma, C.-Q., Parada, M.A., Barra, F., Mittermayr, F. (2013) Pyrite as a record of hydrothermal fluid evolution in a porphyry copper system: A SIMS/EPMA trace element study. *Geochimica et Cosmochimica Acta* 104, 42–62. https://doi.org/10.1016/j.gca.2012.11.006

Román, N., Reich, M., Leisen, M., Morata, D., Barra, F., Deditius, A.P. (2019) Geochemical and micro-textural fingerprints of boiling in pyrite. *Geochimica et Cosmochimica Acta* 246, 60–85. https://doi.org/10.1016/j.gca.2018.11.034

Schaarschmidt, A., Haase, K.M., Klemd, R., Keith, M., Voudouris, P.C., Alfieris, D., Strauss, H., Wiedenbeck, M. (2021) Boiling effects on trace element and sulfur isotope compositions of sulfides in shallow-marine hydrothermal systems: Evidence from Milos Island, Greece. *Chemical Geology* 583, 120457. https://doi.org/10.1016/j.chemgeo.2021.120457

Shore, M., Fowler, A.D. (1996) Oscillatory zoning in minerals; a common phenomenon. *The Canadian Mineralogist* 34, 1111–1126.

Simon, G., Huang, H., Penner-Hahn, J.E., Kesler, S.E., Kao, L.-S. (1999) Oxidation state of gold and arsenic in gold-bearing arsenian pyrite. *American Mineralogist* 84, 1071–1079. https://doi.org/10.2138/am-1999-7-809

Testemale, D., Pokrovski, G.S., Hazemann, J.-L. (2011) Speciation of As^{III} and As^{V} in hydrothermal fluids by *in situ* X-ray absorption spectroscopy. *European Journal of Mineralogy* 23, 379–390. https://doi.org/10.1127/0935-1221/2011/0023-2104

Wu, Y.-F., Fougerouse, D., Evans, K., Reddy, S.M., Saxey, D.W., Guagliardo, P., Li, J.-W. (2019) Gold, arsenic, and copper zoning in pyrite: A record of fluid chemistry and growth kinetics. *Geology* 47, 641–644. https://doi.org/10.1130/G46114.1

Xiao, J., Xie, Z., Xia, Y., Gopon, P., Tan, Q. (2025) Consistent crystal orientation of core and rim pyrites indicates an epitaxial growth of rim in Carlin-type gold deposits. *Geoscience Frontiers* 16, 101966. https://doi.org/10.1016/j.gsf.2024.101966

Xing, Y., Brugger, J., Tomkins, A., Shvarov, Y. (2019) Arsenic evolution as a tool for understanding formation of pyritic gold ores. *Geology* 47, 335–338. https://doi.org/10.1130/G45708.1

Geochemical Perspectives Letters

Pyrite records fluid evolution: sulfur sources controls on arsenic speciation and zonation

A.P. Deditius, X. Yao, F. Xia, J. Brugger, Y. Xing, B. Etschmann, A. Suvorova, M.P. Roberts, C.M. Kewish

Supplementary Information

The Supplementary Information includes:

- Materials and Experiments
- Analytical Methods
- Thermodynamic Modelling
- Tables S-1 to S-6
- Figures S-1 to S-13
- Supplementary Information References

Materials and Experiments

Materials

Euhedral pyrite grains from Navajun Mine in Spain were used as pyrite seeds. The cubes were crushed, sieved into particles 150-355µm, and ultrasonically cleaned in deionised water. Based on the electron probe microanalysis (EPMA) (n = 20), the chemical composition of pyrite is $FeS_{2.03}$, with traces of Ni (~466 ppm) and Cu (~168 ppm) (Table S-1).

The chemicals used were NaH_2PO_4 (≥ 99.0%, Chem-Supply), Na_2HPO_4 (≥ 99.0%, Chem-Supply), NaCl (≥ 99.7%, Chem-Supply), $Fe(NH_4)_2(SO_4)_2 \cdot 6H_2O$ (≥ 98.5%, Merck), NaHS (≥ 99.0%, Sigma-Aldrich), $Na_2S_2O_3 \cdot 5H_2O$ (≥ 99.0%, BOH Chemicals), S (99.3%, Ajax), and As_2O_3 (≥ 99.5%, Chem-Supply).

The pH buffer solution at pH 7 was prepared by dissolving Na_2HPO_4, NaH_2PO_4 and NaCl in Milli-Q water and has a composition of 0.0347 M NaH_2PO_4, 0.0652 M Na_2HPO_4 and 0.6 M NaCl. The pH values were measured by a benchtop pH meter (Eutech pH 2700) with a resolution of 0.01. Calibrations of the pH meter were carried out using standard buffer solutions: pH=4.01 (potassium hydrogen phthalate), pH=7.00 (potassium dihydrogen phosphate and disodium hydrogen phosphate), and pH=10.01 (sodium tetraborate and sodium hydroxide). Dissolved oxygen was removed from the pH buffer solution by purging high-purity N_2 (99.999%) at a rate of 15 mL s^{-1} for 70 min (Butler *et al.*, 1994).

Hydrothermal Experiments

Hydrothermal Synthesis Conditions

The hydrothermal synthesis experiments were conducted in 25 mL polytetrafluoroethylene (PTFE)-lined stainless-steel autoclaves at 200 °C. The specific synthesis conditions are detailed in Table S-2. All sample loadings were performed in an N_2-filled glove box. Once the samples were loaded into the autoclaves, they were tightly sealed before being placed in a preheated oven at 200 °C for the duration of the experiment.

Preparation of Oscillatory-Zoned As-Pyrite

To generate oscillatory zoning in arsenical pyrite (As-pyrite), pyrite seeds (0.15 g; 150–355 µm) were alternately exposed to As-rich and As-free solutions over two full cycles, totalling four experiments. Each experiment lasted 14 days: the first exposure involved the interaction of pyrite seeds in an As-rich solution, followed by the transfer of the reacted seeds into an As-free solution for the same duration. This process was then repeated for a second cycle to develop additional concentric zones.

Transfer of Seeds between Experiments

At the end of each 14-day experiment, the autoclaves were rapidly quenched in cold water before being opened. The solid products were separated from the solution, thoroughly washed with Milli-Q water to remove residual reactants, and dried. Particles larger than 150 µm were retained for the subsequent experimental cycle, ensuring the continued growth of alternating As-rich and As-free layers.

Pyrite Types and Sulfur Sources

Two distinct types of zoned As-pyrite were synthesised using the same iron and arsenic sources but different sulfur sources. Pyrite-S was formed using elemental sulfur (S) and sodium hydrosulfide (NaHS), while pyrite-SO was produced using sodium thiosulfate pentahydrate ($Na_2S_2O_3 \cdot 5H_2O$) and NaHS. In both cases, $Fe(NH_4)_2(SO_4)_2 \cdot 6H_2O$ was used as the iron source, and arsenic was introduced as arsenolite (As_2O_3).

Solution Composition

The composition of the As-free solutions was adapted from Wilkin and Barnes (1996). For Pyrite-S, the As-free solution consisted of 17 mL of pH buffer solution, 0.667 g (1.7 mmol) $Fe(NH_4)_2(SO_4)_2 \cdot 6H_2O$, 0.095 g (1.7 mmol) NaHS, and 0.065 g (2 mmol) elemental sulfur. For Pyrite-SO, the As-free solution contained 17 mL of pH buffer solution, 0.667 g (1.7 mmol) $Fe(NH_4)_2(SO_4)_2 \cdot 6H_2O$, 0.095 g (1.7 mmol) NaHS, and 0.506 g (2 mmol) $Na_2S_2O_3 \cdot 5H_2O$.

The As-rich solutions were prepared by adding 0.024 g (0.12 mmol) As_2O_3 to the respective As-free solutions before the reactor was sealed.

Analytical Methods

The structure, morphology and chemical composition of the starting material and residues were analysed by synchrotron X-ray diffraction (XRD), scanning electron microscopy (SEM), and electron probe microanalyser (EPMA), respectively. The high-resolution structural analyses, as well as distribution and concentrations of As, were investigated using electron back-scattered diffraction (EBSD), selected area diffraction (SAED), transmission electron microscopy (TEM), high-angle annular dark-field (HAADF) scanning TEM, and dispersive X-ray analysis (EDS). The concentrations of As in the solution were measured by ICP-MS. Speciation of As was measured by synchrotron X-ray absorption near-edge structure (XANES). Thermodynamic modelling was conducted using Geochemist's Workbench and HCh. The latter included a non-ideal solid solution model for As uptake by pyrite (Xing *et al.*, 2019b). Pyrite saturation indices were calculated based on the reaction:

$$FeS_2(\text{pyrite}) + 2\,H^+ + H_{2(aq)} = Fe^{2+} + 2\,H_2S_{(aq)};\ \log K_{200\,^\circ C} = 1.451 \quad \text{(Eq. S-1)}$$

XRD analysis and quantification

The XRD analyses of the starting material and the run products were conducted at the powder diffraction beamline at the Australian Synchrotron in Melbourne, Australia, using an X-ray energy of 21 keV (λ=0.5904 Å); the beam energy was calibrated using a LaB_6 standard (NIST SRM 660b). The high-energy beam of the synchrotron source enabled the identification and quantification of the newly precipitated As-pyrite, which was previously unachievable using standard XRD equipment. Quantification of the X-ray diffraction patterns of the product was performed using sequential Rietveld analysis with TOPAS Academic v6, from Coelho Software. In the refinements, the background was modelled using a 5^{th}-order polynomial function. The peaks were modelled using the sums of Gaussian and Lorentzian functions. The starting crystal structure was obtained from the Inorganic Crystal Structure Database (ICSD) (#55699 for pyrite). No other peaks but those of pyrite were detected in the starting mineral sample. The product consisted of either composite grains containing pyrite seed coated with newly formed As-pyrite or particles of As-pyrite only. The content of newly formed As-pyrite in composite particles was obtained based on the analyses of calculated cell parameters for the pyrite seed and particles containing As-pyrite only.

Scanning electron microscopy (SEM)

Scanning electron microscope (SEM) images were obtained on a FEI Verios XHR SEM equipped with an energy dispersive X-ray spectroscopy (EDS) detector (80 mm^2 Oxford Instruments X-Max SDD) for microanalysis. The instrument is located at the Centre for Microscopy, Characterization and Analysis (CMCA) at the University of Western Australia. The pyrite grains were embedded in epoxy resin, polished to expose their cross-sections, coated with a thin carbon film, and imaged under backscattered electron (BSE) mode. BSE images were collected using an acceleration voltage of 10 kV. The EDS analyses were collected using a fully focused beam at an acceleration voltage of 15 kV.

Electron probe microanalysis (EPMA)

Electron probe microanalyses (EPMA) of the samples were carried out using a field-emission JEOL 8530F hyperprobe at the Centre for Microscopy, Characterisation and Analysis (CMCA) at the University of Western Australia. The analyses for the starting pyrite were undertaken using a take-off angle of 40°, an accelerating voltage of 20 kV, and a beam current of 20 nA. X-ray lines, analysing crystals, counting time, and standards used for each element were: S Kα (PETL, 20 s, pyrite), As Kα (TAPL, 20 s, indium arsenide), Fe Kα (LIFL, 20 s, Fe metal), Au Lα (LIFL, 60 s, Au metal), Pb Mα (PETL, 60 s, galena), Cu Kα (LIFL, 60 s, Cu metal), Co Kα (LIFL, 60 s, Co metal), Se Lα (TAPL, 60 s, Se metal), Ni Kα (LIFL, 60 s, Ni metal), Ag Lα (PETL, 60 s, Ag metal), Sb Lα (PETL, 60 s, Sb metal), Te Lα (PETL, 60 s, coloradoite), Hg Mα (PETL, 60 s, coloradoite), Zn Kα (LIFL, 60 s, sphalerite), and Mn Kα (LIFL, 60 s, Mn metal). Detection limits ranged from 0.007 wt. % for Sb to 0.046 wt. % for Au. The same operation conditions were used during single spot analyses and elemental mapping of the products, but only included S Kα (PETL, 20 s, pyrite), As Kα (TAPL, 50 s, indium arsenide), and Fe Kα (LIFL, 20 s, Fe metal). Mean atomic number background corrections were employed throughout (Donovan and Tingle, 1996). Unknown and standard intensities were corrected for dead time, and the ZAF algorithm was used for matrix absorption (Armstrong, 1988). The programs CalcImage v.12.6.2 and Surfer were used for data analysis.

The broad ranges of As concentrations (0.02-6.02 wt.%) in pyrite-S and analytical totals < 100 wt. % stem from a relatively low spatial resolution of the EPMA (excitation volume ~3-5 µm in diameter) and signal contamination from neighbouring areas.

Electron backscatter diffraction (EBSD)

Backscattered electron imaging (BSE) and electron backscattered diffraction (EBSD) were conducted with a FEI Quanta 3D field emission scanning electron microscope (FESEM) at the Monash Centre of Electron Microscope (MCEM), Monash University. Samples for BSE imaging and EBSD were embedded in epoxy resin, polished, and then coated with a thin carbon film (2-4 nm). EBSD patterns were collected at 15 kV and 11 nA with the TSL OIM EBSD system. EBSD data was analysed using TSL-OIM 8 software and the Matlab MTEX toolbox. The Confidence Index (CI) was set to >0.15 to effectively remove low-quality data points. Crystallographic data for pyrite and marcasite were taken from the American Mineralogist Crystal Structure Database (AMCSD).

Transmission electron microscopy (TEM)

The FIB cross-section samples were prepared at the CMCA facility at UWA. A dual-beam FIB-SEM system (FEI Helios NanoLab G3 CX) was used to prepare ultrathin TEM wafers from the resin-embedded polished thin sections coated with c. 20 nm of gold. Electron beam imaging within the dual-beam FIB was used to identify previously mapped microstructures of interest in the thin sections, allowing site-specific TEM samples to be prepared. The TEM sections were prepared by a series of steps involving different ion beam energies (2-30 kV) and currents (40 pA-21 nA) after initial thinning to c. 1 µm. The wafers were extracted using an *in situ* Tungsten micromanipulator and welded onto PELCO FIB-lift-out Cu TEM grids. Final thinning to c. 150 nm was done *in situ* on the grid using lower beam currents. High-angle annular dark field scanning transmission electron microscopy (HAADF-STEM) imaging and element mapping were carried out using a FEI Titan G2 80-200 TEM/STEM with ChemiSTEM Technology operating at 200 kV. The element maps (S, Fe, and As) were obtained by energy-dispersive X-ray spectroscopy using the Super-X detector on the Titan with a probe size of ~1 nm and a probe current of ~0.9 nA.

Inductively coupled-plasma optical emission spectroscopy (ICP-OES)

A Thermo Scientific iCAP^{TM} 7600 inductively coupled plasma optical emission spectrometer was used to determine As concentrations in the solutions after completion of the reactions. The chemical composition of the fluid during the reaction was completed by thermodynamic modelling. Calibration curves for standard solutions at concentrations 1, 5, 20, 50, 100, and 200 ppm were obtained. The sample solutions were diluted to the concentration range of the calibration curves before ICP-OES analysis.

X-ray absorption near-edge spectroscopy (XANES)

Micro-XANES (X-ray absorption near-edge spectroscopy) combined with chemical mapping by micro-XRF (X-ray fluorescence) were used to characterise the chemical state of As in the arsenian pyrites. A micro-beam technique is required to prevent the analysis of As-rich mineral inclusions and assess the homogeneity of the As chemical state. The analyses were conducted at the X-ray fluorescence microscopy beamline (XFM; Howard *et al.*, 2020) on polished pyrite grains embedded in epoxy resin, at the Australia Synchrotron, Melbourne, Australia. Details of the measurement procedure and data reduction can be found in Li *et al.* (2016) and Etschmann *et al.* (2014). The incident beam energy was set at 12.117 keV using a horizontal Si(111) monochromator with an energy resolution $\Delta E/E$ of ~2.8×10^{-4}. This energy corresponds to the highest energy in the XANES stacks and provides optimum detection limits for As. The beam was focused to a ~2x2 µm^2 spot size using Kirkpatrick-Baez mirrors. Full spectral fluorescence data (as opposed to only regions-of-interest) were collected using the Maia model D384 detector array, which has an energy resolution of 240 eV (Ryan *et al.*, 2014). Samples were mapped in continuous mode using scanning speeds ranging from 0.5-1 mm/s for mapping, corresponding to dwell times of 0.75 to 1.5 ms/pixel. The full spectral data were analysed using GeoPIXE II (Ryan, *et al.*, 1996, 2010), using the Dynamic Analysis method (DAM) (Ryan, 2000), which subtracts background, escape peaks and other detector artefacts. Standard foils (Pt, Mn, Fe) were used as external standards to constrain the quantification parameters (detector geometry and efficiency; ion chamber calibration to measure photon flux). Note that As concentrations are semi-quantitative only because As is located on the edge of the grains, and sample thickness varies; this affects the accuracy of the corrections for the absorption effect and the fluorescence excitation (performed assuming a fixed pyrite thickness of 50 µm).

The chemical state of As was mapped using XANES imaging, as described in Etschmann *et al.* (2010, 2014). Grains for measurements were selected based on the overview maps of each sample. XANES stacks were measured by collecting µSXRF maps/lines at 82 irregularly spaced monochromator energies that spanned the As-K edge, with 0.5 eV steps across the edge. A separate Dynamic Analysis matrix was used for each beam energy when processing the stack to track the changing energy of the scatter peaks. The intensities of the As Kα peak, integrated over regions in the µSXRF map, were extracted and used to construct XANES spectra at each monochromator energy. X-ray excitation volume was 2 µm x 2 µm horizontal resolution.

XANES maps were obtained on Pyrite-S (two grains, total 148 kpixel, with ~9,000 pixels/map As-rich) and Pyrite-SO (two grains, total 240 kpixel, including ~20,000 pixels/map As-rich) at pixel sizes of 2x2 and 1x1 µm^2, respectively. In

each map, sample heterogeneity was investigated by extracting pixels with different ratios of emission intensities at energies near the white line maximum (Table S-4, *e.g.*, Ram *et al.*, 2019) and as a function of As concentrations. In the case of line scans, the reported standard deviation is that of the centroid of the white line in each pixel, determined by fitting a Gaussian around the peak maximum.

Thermodynamic Modelling

The thermodynamic calculations for the titration of different sulfur sources to precipitate pyrite were conducted using the HCh software package (Shvarov and Bastrakov, 1999), which uses a Gibbs free energy minimisation algorithm to calculate the equilibrium of mineral-fluid systems. Calculations at water densities above 0.35 g/cm^3 and a P-T range of 0-1000 ºC and 0-5000 bar are possible, in agreement with the limitations imposed by the HKF equation of state (EoS) used for aqueous species (Tanger and Helgeson, 1988; Johnson *et al*., 1992). The thermodynamic properties of aqueous species and minerals were collected from an updated version of the Unitherm database (Shvarov, 1999; Xing *et al.*, 2019a). In particular, the non-ideal solid solution model of As in pyrite and arsenopyrite, developed by Xing *et al.* (2019b), was used to accurately predict As incorporation into pyrite. We use the standard states for aqueous species, which is the hypothetical 1 molal at infinite dilution, *i.e.* $\boldsymbol{\gamma = 1}$ at infinite dilution at any given pressure and temperature. For minerals, the standard state is the pure stoichiometric phase. In the case of the FeS_2-$FeAs_2$ solid solution, we use Henry's law standard state for the dilute component, *i.e.* $\boldsymbol{\gamma}$ ($FeAs_2$) = $\boldsymbol{\gamma}$ (FeS_2) = 1 in an As-poor arsenian pyrite.

Figure 4 was calculated using HCh software based on the database as mentioned above. The initial composition of the titration system used in the model was based on the experimental setup of this study and is provided in Table S6. The Aliquot-Type model (Xing *et al.*, 2018) was used to simulate the titration process by gradually increasing the amount of either $Na_2S_2O_3$ or native sulfur (S) in the initial system (Table S-6). The calculation was performed at 200 ºC with vapour saturation pressure consistent with the experimental setup. The calculated data was processed in Matlab for visualisation. The calculated saturation index of pyrite, as presented in Figure S-10, was extracted from this modelling result as well.

The activity-activity diagrams, as shown in Figure S-9, were calculated using the Geochemist's Workbench. The database used for the calculation is based on the common thermodynamic data from the SUPCRT database for aqueous species and minerals (Johnson *et al.*, 1992; Shock *et al.*, 1997; Sverjensky *et al.*, 1997), which is consistent with the thermodynamic data from the Unitherm database used in HCh. For both Figure S-9a and Figure S-9b, the calculation was performed at 200 ºC with a vapour saturation pressure.

Supplementary Tables

Table S-1 EPMA single-point analyses of starting pyrite (n=20).

Element	Detection limit	wt.% mean (range)
S	0.005	53.89 (53.72–54.19)
As	0.011	bdl
Sb	0.009	bdl
Fe	0.01	46.39 (46.19–46.67)
Se	0.021	bdl
Au	0.03	bdl
Te	0.009	bdl
Cu	0.007	0.02 (0.01–0.02)
Pb	0.013	bdl
Ni	0.006	0.05 (0.01–0.11)
Co	0.003	bdl
Ag	0.007	bdl
Hg	0.015	bdl
Zn	0.009	bdl
Mn	0.006	bdl
Total		100.35

bdl: below the detection limit.

Table S-2 Summary of the experimental conditions and the calculated chemical speciation in the aqueous fluids at equilibrium.

Solid sample from the experiments	Exp.	Starting seeds	Composition of the fluid system (numbers of moles of substance per kg fluid, m)	T (°C)	t (days)	pH 7 buffer[a] (mL)	pH[d]	SI (S^0)[e]	SI_{py} (FeS_2)[f]	H_2S (m)	SO_2 (m)	ΣSO_4[g] (m)	$S_3^{\cdot-}$ +$S_2^{\cdot-}$ (m)
Pyrite-S_1	1	Pyrite (0.15 g, 150-355 um)	NaCl(0.55), NaH_2PO_4(0.03), Na_2HPO_4(0.06), $Fe(NH_4)_2(SO_4)_2{\cdot}6H_2O$(0.09), NaHS(0.09), S(0.11)[b], As_2O_3(0.006)	200	14	17	3.796	-0.298	0.496	1.14E-02	2.53E-06	0.205	2.97E-06
Pyrite-S_2	2	Pyrite-S_1	NaCl(0.55), NaH_2PO_4(0.03), Na_2HPO_4(0.06), $Fe(NH_4)_2(SO_4)_2{\cdot}6H_2O$(0.09), NaHS(0.09), S(0.11)[b]	200	14	17	3.803	-0.235	0.496	1.40E-02	2.60E-06	0.205	4.80E-06
Pyrite-S_3	3	Pyrite-S_2	NaCl(0.55), NaH_2PO_4(0.03), Na_2HPO_4(0.06), $Fe(NH_4)_2(SO_4)_2{\cdot}6H_2O$(0.09), NaHS(0.09), S(0.11)[b], As_2O_3(0.006)	200	14	17	3.796	-0.298	0.496	1.14E-02	2.53E-06	0.205	2.97E-06
Pyrite-S	4	Pyrite-S_3	NaCl(0.55), NaH_2PO_4(0.03), Na_2HPO_4(0.06), $Fe(NH_4)_2(SO_4)_2{\cdot}6H_2O$(0.09), NaHS(0.09), S(0.11)[b]	200	14	17	3.803	-0.235	0.496	1.40E-02	2.60E-06	0.205	4.80E-06
Pyrite-SO_1	1	Pyrite (0.15 g, 150-355 um)	NaCl(0.53), NaH_2PO_4(0.03), Na_2HPO_4(0.06), $Fe(NH_4)_2(SO_4)_2{\cdot}6H_2O$(0.09), NaHS(0.09), $Na_2S_2O_3{\cdot}5H_2O$(0.11)[c], As_2O_3(0.006)	200	14	17	4.906	-0.625	0.496	2.05E-02	8.36E-08	0.292	7.92E-06
Pyrite-SO_2	2	Pyrite-SO_1	NaCl(0.53), NaH_2PO_4(0.03), Na_2HPO_4(0.06), $Fe(NH_4)_2(SO_4)_2{\cdot}6H_2O$(0.09), NaHS(0.09), $Na_2S_2O_3{\cdot}5H_2O$(0.11)[c]	200	14	17	5.057	-0.472	0.496	4.13E-02	5.94E-08	0.292	3.85E-05
Pyrite-SO_3	3	Pyrite-SO_2	NaCl(0.53), NaH_2PO_4(0.03), Na_2HPO_4(0.06), $Fe(NH_4)_2(SO_4)_2{\cdot}6H_2O$(0.09), NaHS(0.09), $Na_2S_2O_3{\cdot}5H_2O$(0.11)[c], As_2O_3(0.006)	200	14	17	4.906	-0.625	0.496	2.05E-02	8.36E-08	0.292	7.92E-06
Pyrite-SO	4	Pyrite-SO_3	NaCl(0.53), NaH_2PO_4(0.03), Na_2HPO_4(0.06), $Fe(NH_4)_2(SO_4)_2{\cdot}6H_2O$(0.09), NaHS(0.09), $Na_2S_2O_3{\cdot}5H_2O$(0.11)[c]	200	14	17	5.057	-0.472	0.496	4.13E-02	5.94E-08	0.292	3.85E-05

[a] pH 7 buffer: 0.0347 M NaH_2PO_4 + 0.0652 M Na_2HPO_4 + 0.6 M NaCl.
[b] The starting composition of the system in each experiment is the same except for the concentration of As_2O_3.
[c] $Na_2S_2O_3{\times}5H_2O$ as the source of S.
[d] Calculated pH of the experiment.
[e] Calculated saturation index SI (S^0) = $0.5\log_{10}(H^+) + 0.75\log_{10}(H_2S) + 0.25\log_{10}(SO_4^{2-}) - \log_{10}(K)$.
[f] Calculated saturation index of pyrite SI_{py} (FeS_2) = $\log_{10}(Fe^{2+}) + 2{*}\log_{10}(H_2S) - 2\log_{10}(H^+) - \log_{10}(H_{2aq}) - \log_{10}K$.
[g] Sum of sulfate-type species.

Table S-3 The results of EPMA and TEM-EDS analyses of the products.

	Pyrite-S				Pyrite-SO			
	Fe (wt.%)	S (wt.%)	As (wt.%)	Total (wt.%)	Fe (wt.%)	S (wt.%)	As (wt.%)	Total (wt.%)
EPMA results	45.16	53.04	bdl	98.19	45.16	53.04	bdl	98.19
	45.16	53.04	bdl	98.19	45.35	52.85	bdl	98.21
	45.35	52.85	bdl	98.21	45.35	52.79	bdl	98.14
	45.35	52.85	bdl	98.21	45.5	53.63	bdl	99.15
	45.35	52.79	bdl	98.14	45.24	53.7	bdl	98.96
	45.35	52.79	bdl	98.14	45.85	52.86	0.02	98.73
	47.88	50.68	bdl	98.57	45.85	52.86	0.02	98.73
	47.1	52.34	bdl	99.45	45.8	54.08	0.05	99.93
	45.5	53.63	bdl	99.15	45.73	52.88	0.08	98.62
	45.5	53.63	bdl	99.15	45.16	53.64	0.08	98.88
	45.24	53.7	bdl	98.96	45.16	53.64	0.08	98.88
	45.24	53.7	bdl	98.96	45.35	52.85	0.11	98.31
	45.85	52.86	0.02	98.73	45	52.36	0.13	97.49
	45.85	52.86	0.02	98.73	46	52.36	0.13	98.49
	45.85	52.86	0.02	98.73	44.73	53.25	0.14	98.12
	45.85	52.86	0.02	98.73	44.73	53.25	0.14	98.12
	46.39	53.04	0.02	99.45	44.69	54.01	0.15	98.86
	46.59	53.12	0.02	99.73	45.71	52.56	0.15	98.27
	46.53	53.13	0.02	99.68	44.49	53.75	0.17	98.41
	45.98	52.53	0.04	98.55	44.49	53.75	0.17	98.41
	45.8	54.08	0.05	99.93	45.83	53.06	0.18	98.99
	45.8	54.08	0.05	99.93	46.56	52.3	0.21	99.08
	47.47	50.66	0.06	98.19	44.77	54.33	0.21	99.31
	46.54	52.06	0.07	98.67	45.31	53.05	0.26	98.56
	45.28	52.11	0.07	97.47	44.23	53.46	0.28	97.97
	46.04	51.89	0.14	98.07	46.23	53.46	0.28	99.97
	46.15	53	0.2	99.15	46.38	52.86	0.32	99.54
	46.09	53.24	0.22	99.34	45.49	52.9	0.36	98.79
	46.35	53.23	0.23	99.81	45.95	52.13	0.37	98.45
	46.47	53.05	0.27	99.53	45.73	52.52	0.4	98.64
	46	52.55	0.28	98.55	46.03	51.21	0.41	97.84
	46.42	53.01	0.3	99.43	45.58	53.36	0.42	99.45
	48.05	51.16	0.31	99.52	45.11	53.11	0.52	98.74
	45.76	52.55	0.31	98.61	46.03	53.05	0.55	99.64
	46.28	53.03	0.56	99.32	44	53.61	0.56	98.17
	46.05	52.95	0.67	99.67	45.72	53.01	0.59	99.33
	46.19	52.87	0.72	99.78	45.99	52.86	0.61	99.44
	45.97	52.25	0.82	99.04	45.71	53.38	0.61	99.68
	48.13	49.95	1.07	99.15	45.92	52.46	0.69	99.08

Table S-3 continued.

	Pyrite-S				Pyrite-SO			
	Fe (wt.%)	S (wt.%)	As (wt.%)	Total (wt.%)	Fe (wt.%)	S (wt.%)	As (wt.%)	Total (wt.%)
EPMA results	44.94	51.75	1.11	97.8	46.31	52.87	0.71	99.89
	45.39	51.6	1.18	98.18	46.02	52.72	0.77	99.54
	45.54	51.81	1.28	98.63	46.08	52.94	0.8	99.82
	46.34	52.09	1.39	99.82	45.96	52.81	0.88	99.65
	46.33	52.17	1.39	99.9	46.05	52.8	0.91	99.85
	45.04	50.44	2.31	97.79	44.74	52.56	0.98	98.3
	45.86	50.36	2.38	98.6	44.61	52.85	1	98.46
	45.51	50.89	2.39	98.8	44.56	52.3	1.21	98.08
	45.14	50.74	3.03	98.91				
	46.06	49.26	4.05	99.38				
	45.22	50.43	4.18	99.83				
	45.6	48.37	4.22	98.19				
	45.36	48.15	5.05	98.56				
	45.85	48.77	5.21	99.83				
	45.48	48.38	5.27	99.13				
	45.22	48.41	5.45	99.08				
	45.79	47.93	5.86	99.57				
	44.1	49.59	6.02	99.71				
TEM-EDS Results	46.5	48.3	5.2	100	46.5	53.4	0.2	100
	46	48.5	5.5	100	46.8	52.9	0.3	100
	46.3	48.2	5.5	100	46.7	52.9	0.4	100
	46	48.3	5.8	100	45.1	54.3	0.6	100
	47.3	52.7	0	100	45.3	54	0.7	100
	47.5	52.5	0	100	45.7	53.2	1.1	100
	47.7	52.2	0.1	100	44.6	54.1	1.3	100
	47.3	52.6	0.1	100	45.3	53.4	1.3	100
	46.8	48.6	4.6	100	45	53.6	1.4	100
	46.9	48.5	4.6	100	44	54.6	1.4	100
	46.5	48.8	4.7	100	45.6	53.1	1.4	100
	46.6	48.8	4.7	100	44.5	54.1	1.4	100
	47.9	51.3	0.8	100	45.3	53.2	1.5	100
	48	51.2	0.8	100				
	48.2	50.9	0.9	100				
	47.8	51.3	0.9	100				
	47.6	52.4	0	100				
	47.5	52.5	0	100				
	47.2	52.8	0	100				
	47.3	52.6	0	100				

Table S-4 The mean position of white line (peak of the absorption edge) energies in eV for arsenical groups in created arsenian pyrites and selected reference materials.

Sample	White line	Standard deviation	Interpretation	Number of measurements/types of XANES dataset
Pyrite-S	11,869.80	0.06	$[As_2]^{2-}$ for $[S_2]^{2-}$	~9,000 pixels/map
Pyrite-SO	11,870.20	0.03	$As^{2+/3+}$ for Fe^{2+}	~20,000 pixels/map
As_2O_3	11,871.70	-	As^{3+}	Smith *et al*. (2005)
AsS (realgar)	11,870.13		As^{2+}	James-Smith *et al.* (2010)
FeAsS (arsenopyrite)	11,869.17	-	As^{2-}	James-Smith *et al.* (2010)

Table S-5 The arsenic weight ratio between the newly formed As-pyrite and the fluid.

As-Pyrite	As in starting solution (ppm)	As ratio[1] (solid/fluid)	As ratio[2] (solid/fluid)	As ratio[3] (solid/fluid)
Pyrite-S	1069	11.63	14.87	110.93
Pyrite-SO	1069	11.78	20.37	48.29

[1] The As weight of the solid is obtained from the EPMA results of all zones, while the As weight of the solution is acquired from ICP-OES results of the remaining solution after producing Zone-1.
[2] The As weight of the solid is obtained from the EPMA results of all zones, while the As weight of the solution is acquired from ICP-OES results of the remaining solution after producing Zone-3.
[3] The As weight of the solid is obtained from the TEM EDS results of Zone-1, while the As weight of the solution is acquired from ICP-OES results of the remaining solution after producing Zone-1.

Table S-6 Initial composition of the system used to simulate the titration of $Na_2S_2O_3$ and native sulfur.

Component	Amount
H_2O	1 kg
As_2O_3	0.05 mol
$FeSO_4$	0.1 mol
NaCl	0.5 mol
NaHS	0.1 mol
$(NH_4)_2SO_4$	0.1 mol
NaOH	0.06 mol

Supplementary Figures

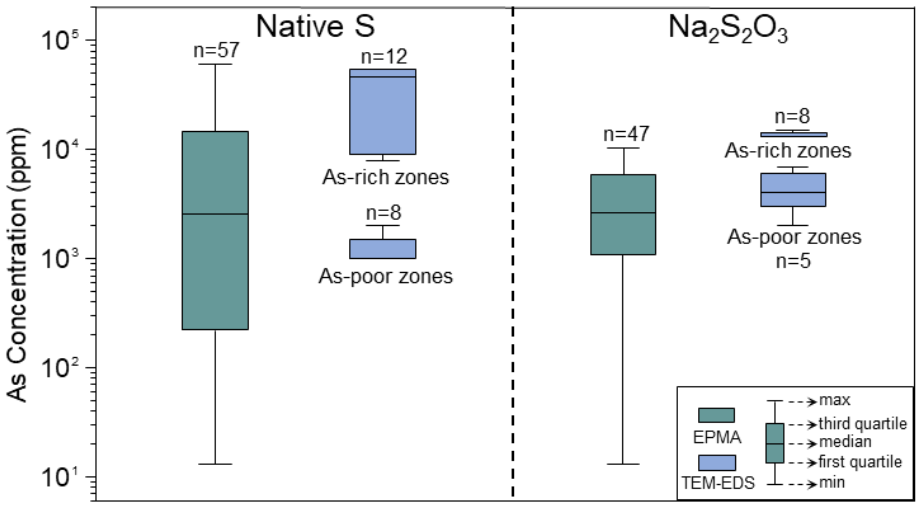

Figure S-1 Concentration plot for As in newly-formed pyrite. EMPA and TEM EDS spot analysis data are included and displayed as boxplots separately (green and blue boxes correspond to the results of EPMA and TEM analyses, respectively). Data are plotted in parts per million (ppm) on a vertical logarithmic scale. In each boxplot, minimum, median, and maximum concentrations are marked, and the number of single-point analyses is shown at the top.

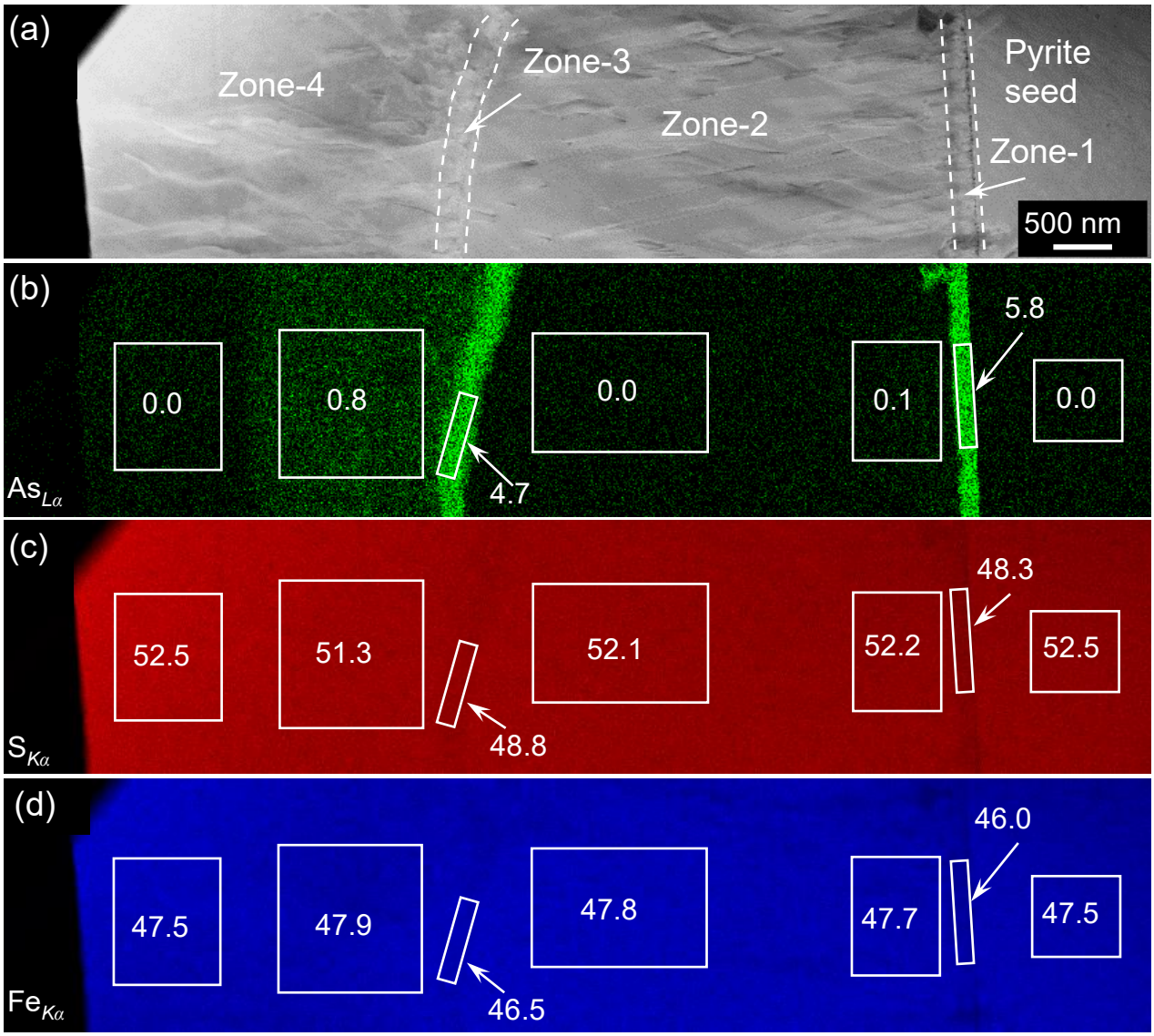

Figure S-2 **(a)** HAADF-TEM image of the oscillatory zoned As-pyrite formed on the pyrite seed. **(b-d)** EDS elemental mapping of As, S, and Fe, respectively. The rectangles and the values represent the areas of analysis and the concentration of the elements (in wt.%). Experimental conditions: 200 °C, anoxic conditions for 8 weeks, As_2O_3 as the source of As, and elemental S as the source of sulfur (see also Fig. S-11 for the As analyses in Zone-2).

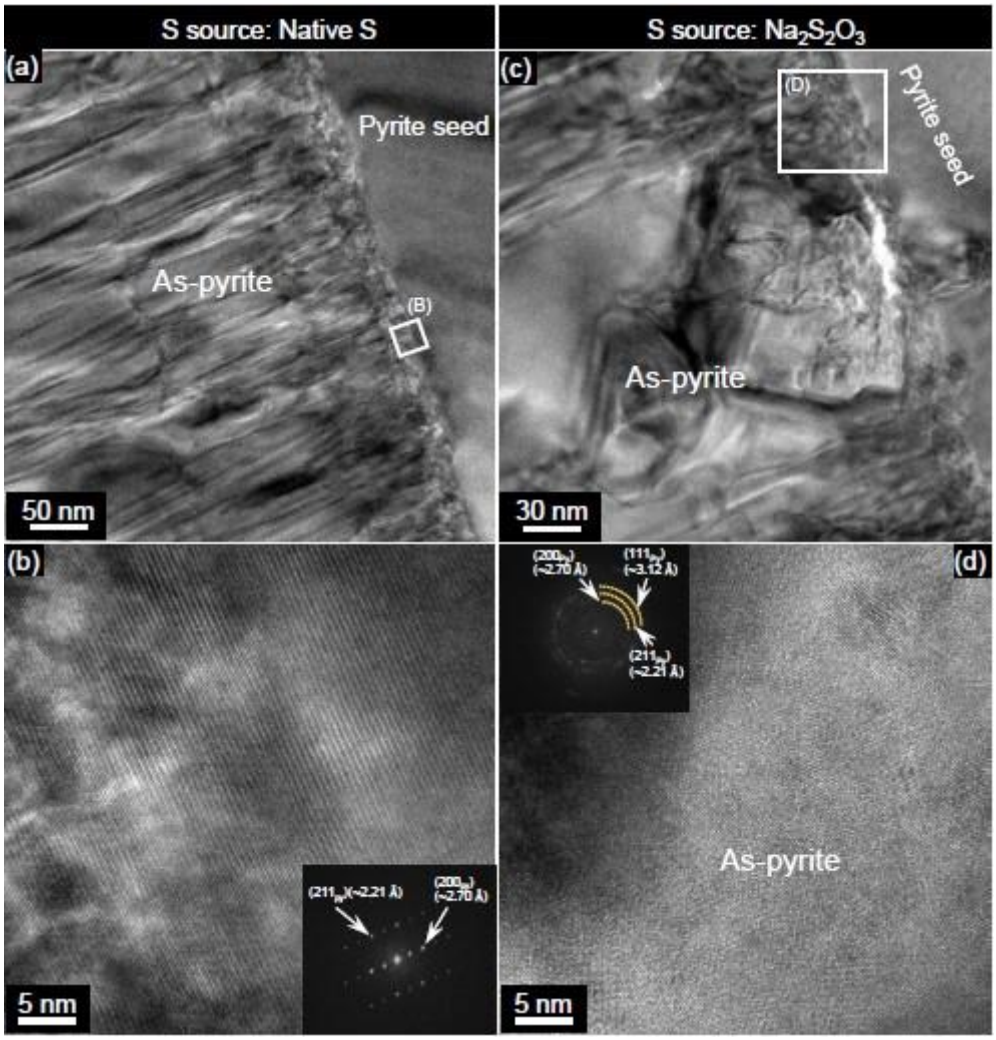

Figure S-3 **(a-b)** HRTEM image of the contact between As-pyrite-S (Zone-1) and pyrite seed. FFT diffraction pattern in **(b)** documents a single crystal, *i.e.* epitaxial growth of pyrite-S. **(c-d)** Randomly oriented grains of As-pyrite-SO and ring diffraction pattern with *d*-spacing of pyrite. Py: pyrite.

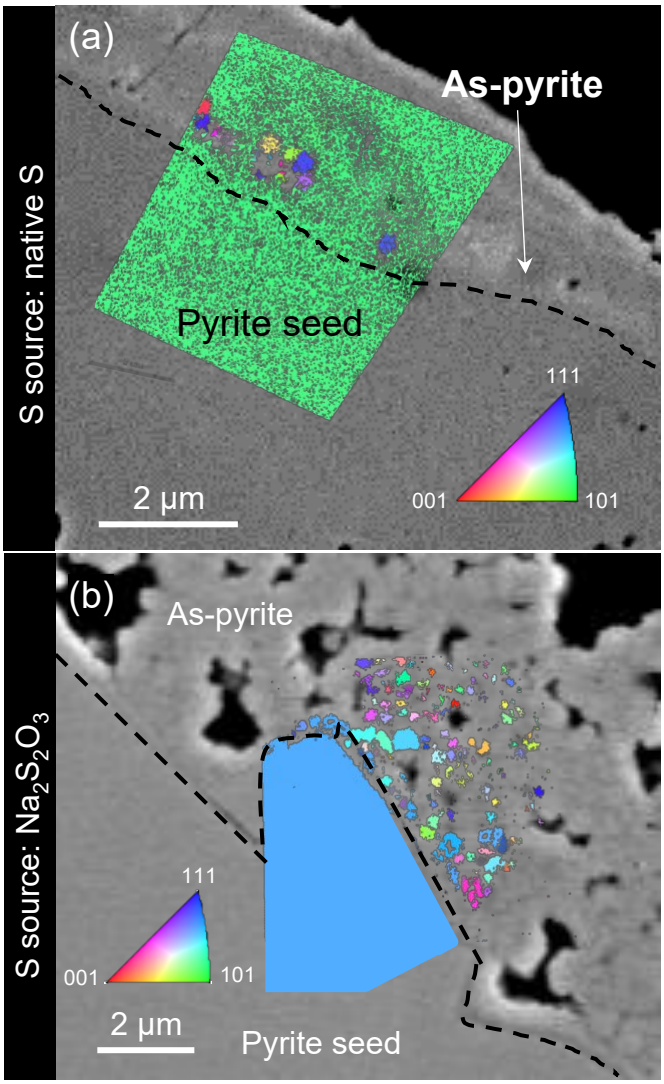

Figure S-4 EBSD analysis of the grain boundary between pyrite seed and the newly formed arsenian pyrite overlapped with BSE images (Experimental conditions: 200 °C, anoxic condition for 8 weeks, **(a)** native S and **(b)** $Na_2S_2O_3$ as the source of sulfur). **(a)** Note the same orientation of pyrite seed and the alternate As-rich (brighter in BSE) and As-poor zoning of newly formed pyrite (pyrite-S); **(b)** note the random orientation of porous aggregates of As-pyrite (pyrite-SO). The colours correspond to different crystallite orientations concerning the surface normal, as indicated by the associated colour key.

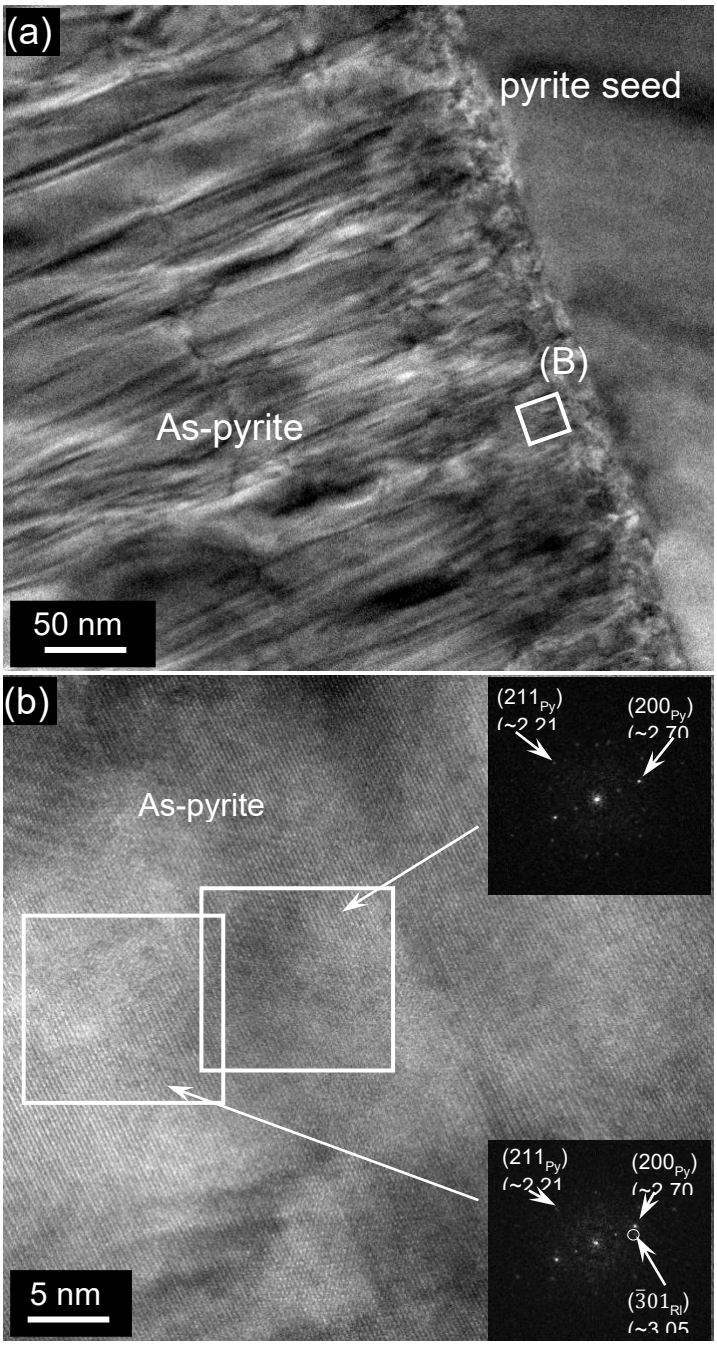

Figure S-5 TEM images of As-pyrite and pyrite seed. **(a)** Low-magnification bright-field TEM images of the grain boundary between the pyrite seed and the newly formed As-pyrite. **(b)** High-resolution TEM image of the boundary between As-pyrite and pyrite seed associated with Fast Fourier Transform (FFT) diffraction pattern that indicates a single crystal of pyrite; FFT shows diffraction pattern with *d*-spacing of realgar. Note that the source of sulfur for figures is native S. Py - pyrite and Rl - realgar.

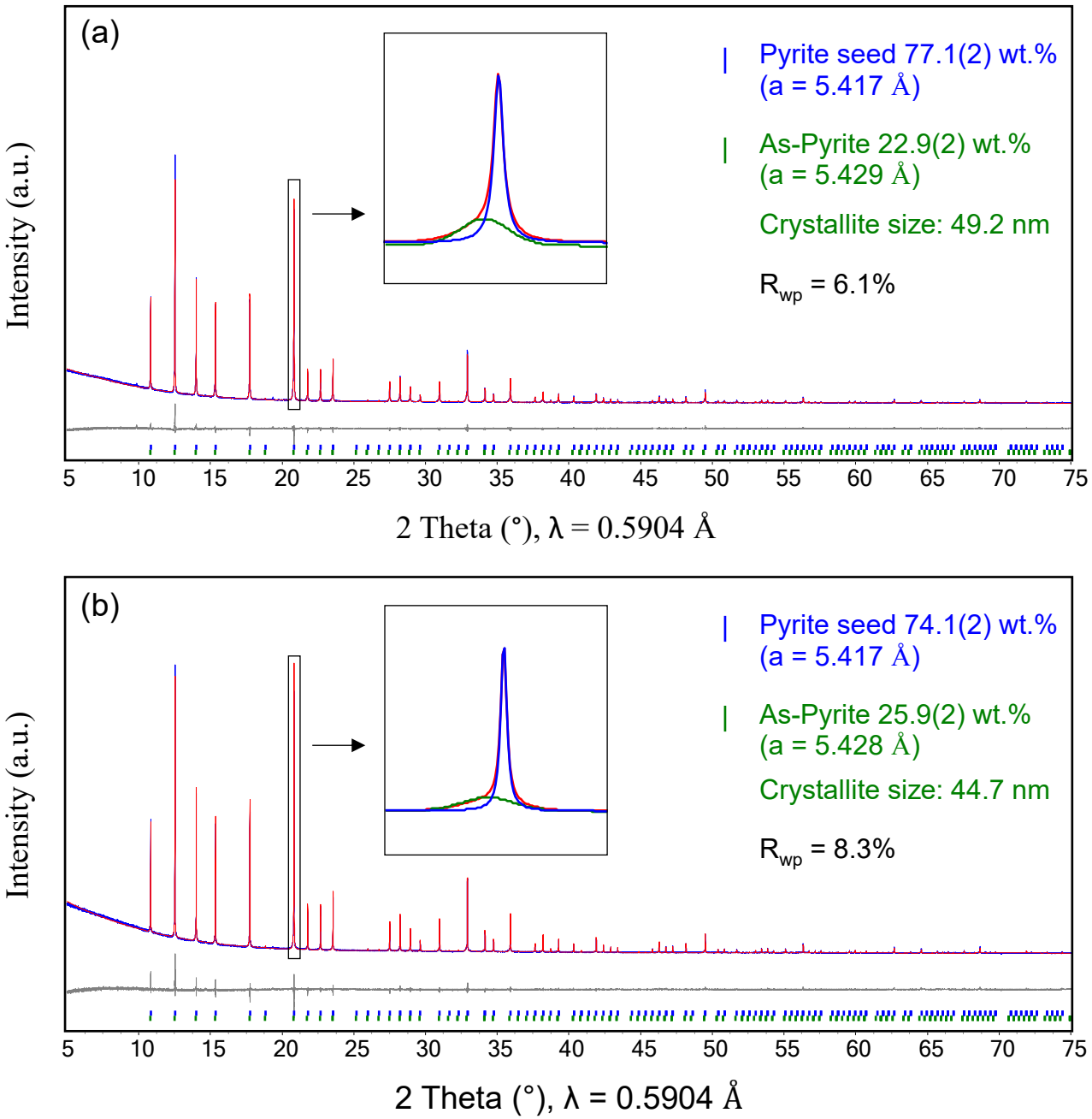

Figure S-6 Synchrotron-XRD patterns and Rietveld refinement analyses of arsenian pyrite after four consecutive experiments of growth on pyrite seeds (200 °C, anoxic conditions, 8 weeks), using **(a)** native S and **(b)** $Na_2S_2O_3$ as the source of sulfur. Note: the insets (20.82º to 21.04º) show the (311) peak, including a broad peak (green) from nanocrystalline arsenian pyrite and a sharp peak (blue) from pyrite seed.

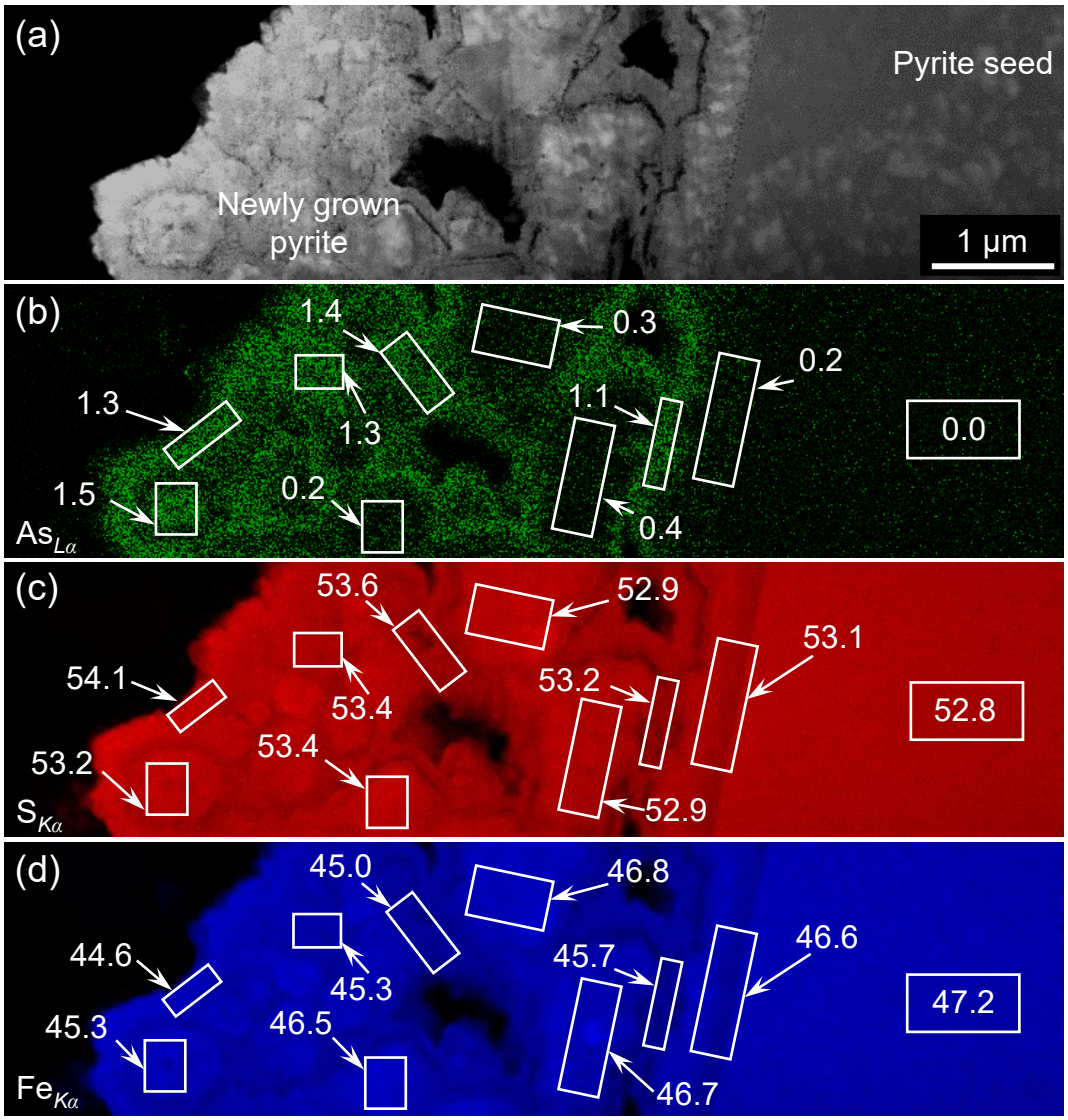

Figure S-7 **(a)** HAADF-STEM image of concentric aggregates of As-pyrite growth on a pyrite seed. **(b-d)** EDS elemental mapping of As, S, and Fe, respectively. Experimental conditions: 200 °C, under anoxic conditions for 8 weeks, with As_2O_3 as the source of As and $Na_2S_2O_3$ as the source of sulfur. The rectangles represent the areas of analysis, and the numbers indicate the concentration of the element (in wt.%).

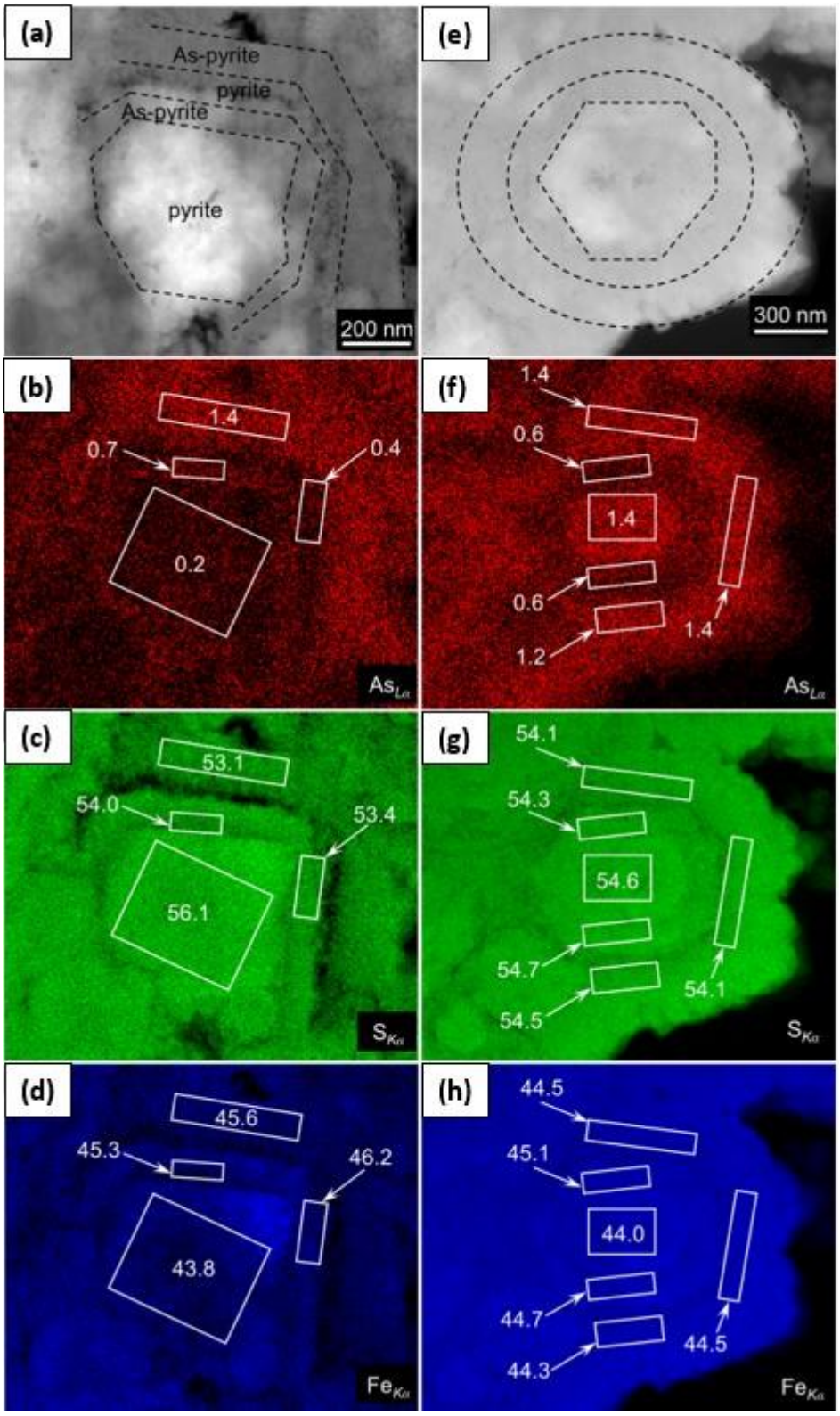

Figure S-8 **(a and e)** HAADF-STEM image of concentric aggregates of As-pyrite growth on pyrite seed. **(b-d and f-h)** EDS elemental mapping of As, S, and Fe, respectively. Experimental conditions: 200 °C, anoxic conditions for 8 weeks, $Na_2S_2O_3$ as the source of sulfur. The rectangles represent the areas of analysis, and the numbers indicate the concentration of the element (in wt.%).

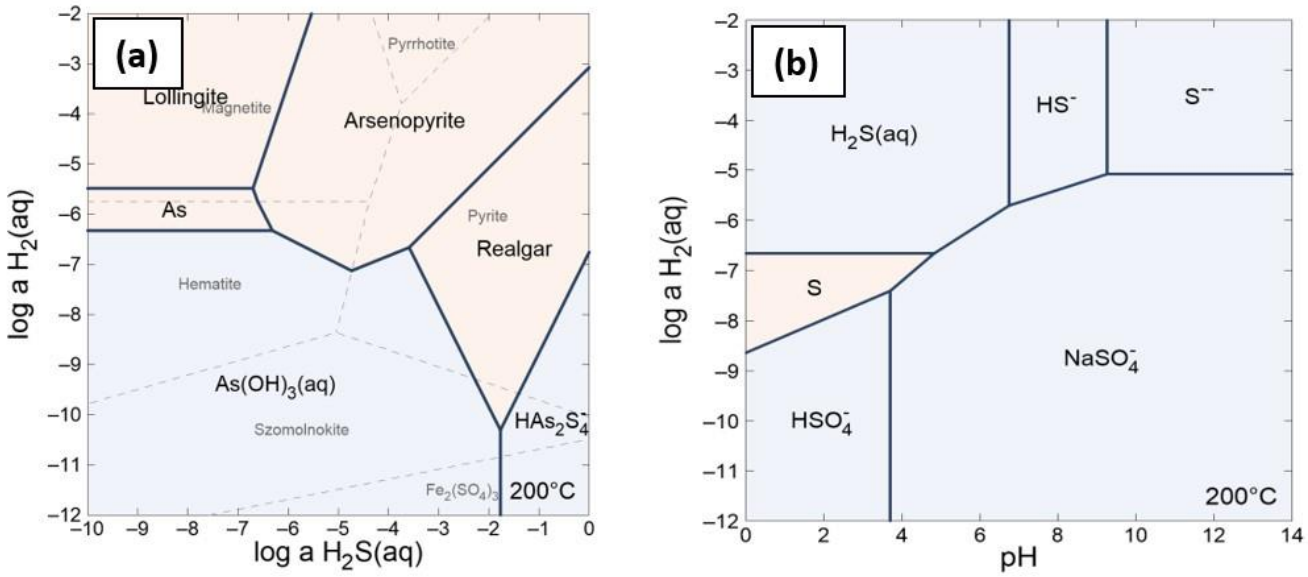

Figure S-9 Arsenic **(a)** and sulfur **(b)** speciation as a function of the activity of H_2(aq) and H_2S(aq). The calculation of the activity diagrams was performed with the Geochemist's Workbench.

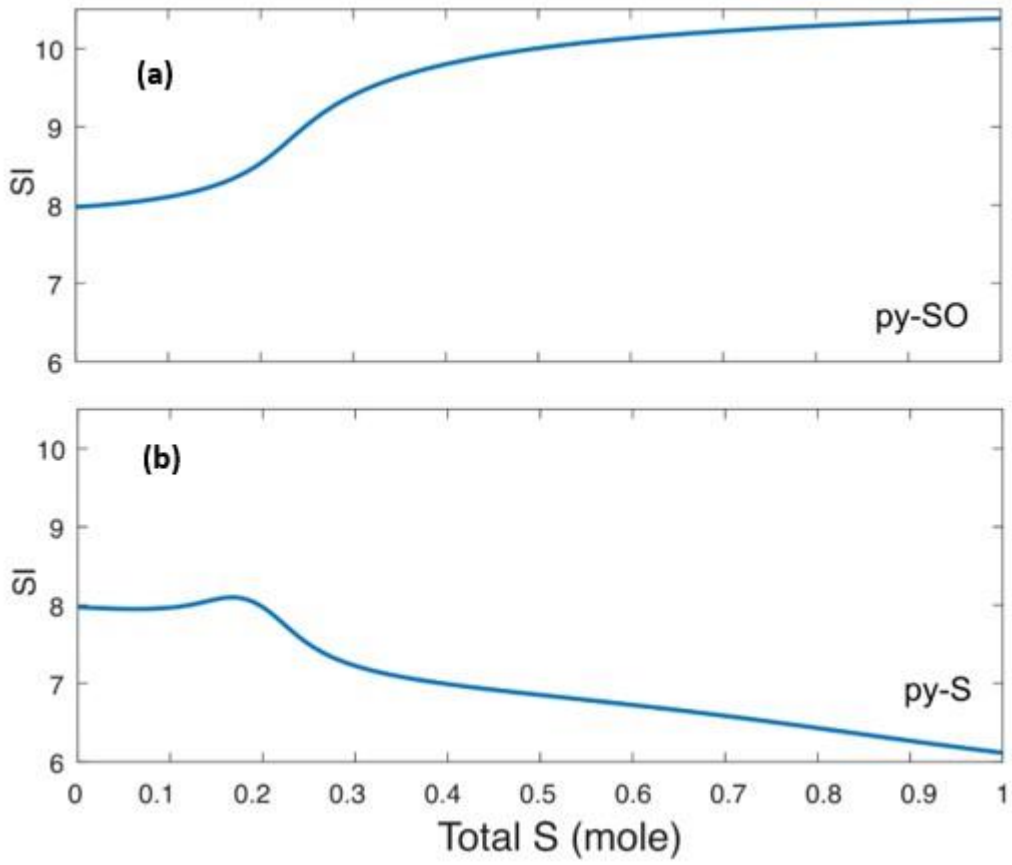

Figure S-10 Calculated saturation index (SI) of pyrite when titrating $Na_2S_2O_3$ **(a)** or native S **(b)**. **(a)** the SI increases with an increasing amount of total S; **(b)** the SI decreases with the increasing amount of S.

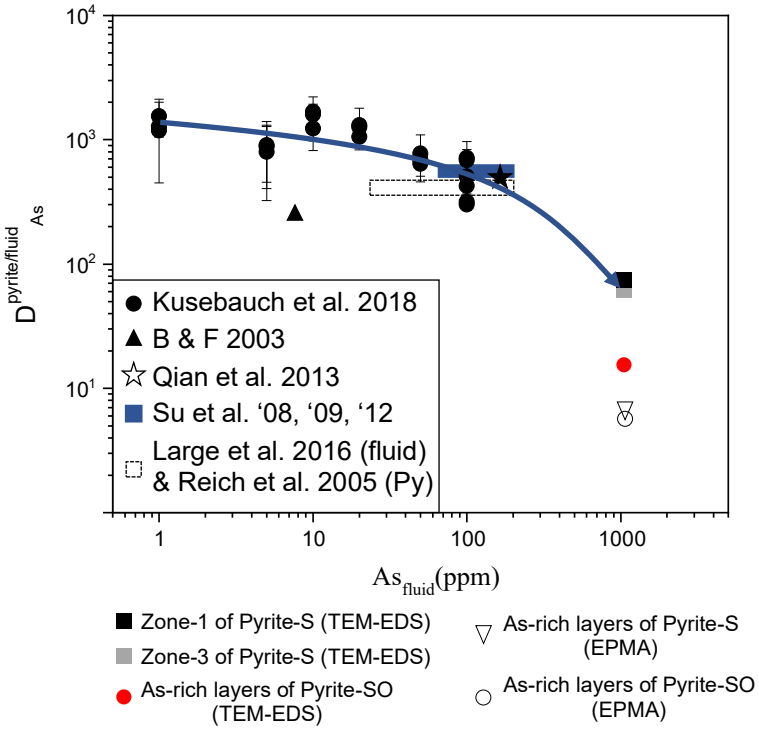

Figure S-11 Comparison of the partitioning coefficient ($D_{py/fluid}$) values from this study with published values as a function of As concentration in the fluid (modified after Kusebauch *et al.*, 2018). Note the decreasing trend of D values with increasing concentration of As in the fluid (blue arrow), which indicates the decrease of As uptake by pyrite with increasing As concentration. Values are calculated based on data in Table S-4. The intergrowth of pyrite with realgar has only a minute effect on the $D_{py/fluid}$, Zone-1 with realgar vs. Zone-3 without. 'B & F' stands for Bostick and Fendorf (2003).

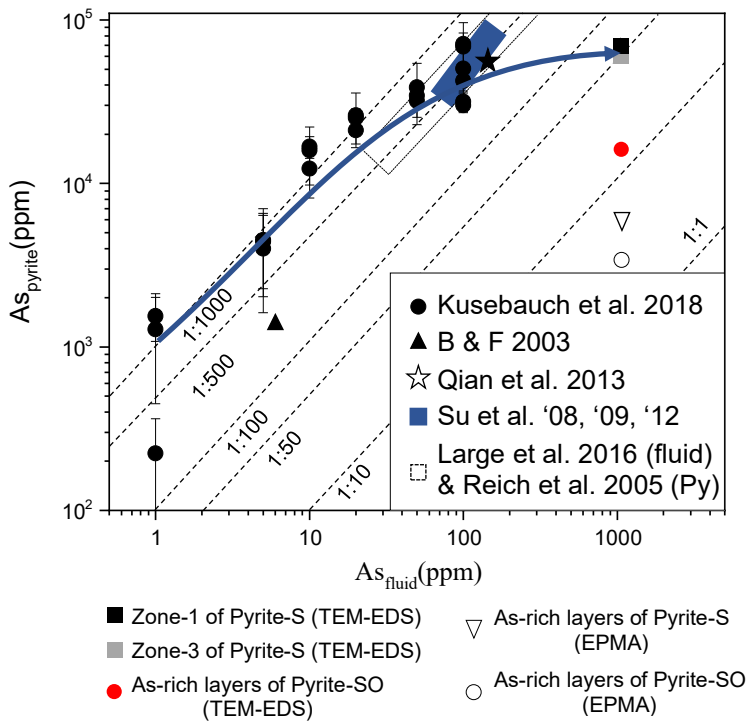

Figure S-12 Comparison of the concentration of As in pyrite as a function of As concentration in the starting fluid in this study with literature data (Filled symbols show TEM-EDS analyses; open symbols show EPMA analyses. Squares are the experiments with native sulfur; circles are the experiments with $Na_2S_2O_3$. Black and grey filled squares represent Zone-1 and Zone-3a, respectively; the red filled circle shows analyses of As-rich zones in microparticulate pyrite. Note the increase in the As concentration in pyrite with increasing As concentration in the fluid up to ~100 ppm As_{fluid}. No increase has been observed (blue arrow) at 10^3 concentrations of As in the fluid, which suggests that the maximum solubility of As has been achieved. Modified after Kusebauch *et al.* (2018). 'B & F' stands for Bostick and Fendorf (2003).

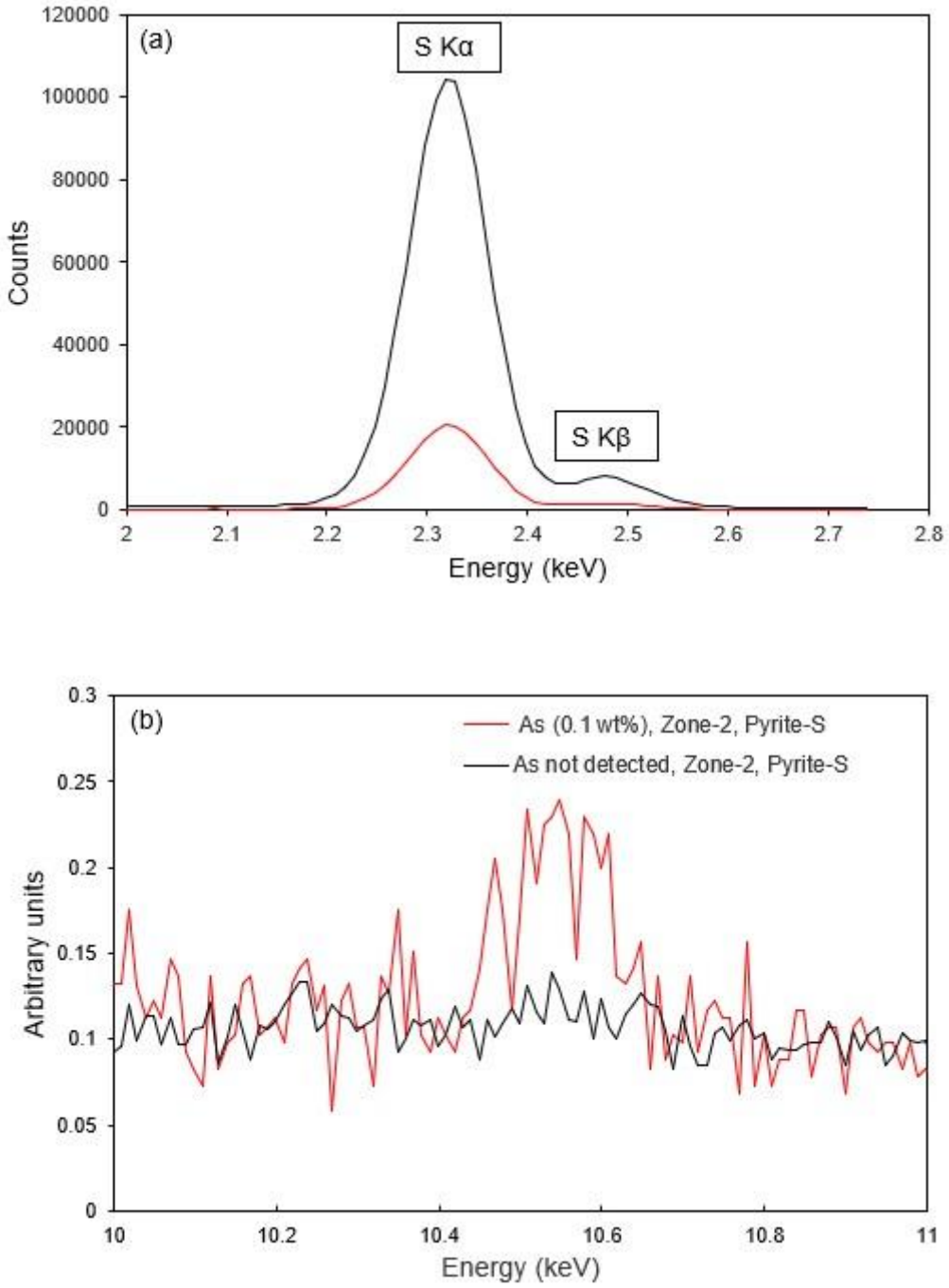

Figure S-13 **(a-b)** EDS spectra of pyrite containing 0.1 wt.% of As and pyrite without a detectable amount of As in Zone-2, Pyrite-S (see Fig. S2 for the position of the analyses). Spectra normalised against the respective intensities of the S Kα peak **(a)**.

Supplementary Information References

Armstrong, J.T. (1988) Quantitative analysis of silicates and oxide minerals: Comparison of Monte-Carlo, ZAF and ϕ(ρz) procedures. In: Newbury, D.E. (Ed.) *Microbeam Analysis*. San Francisco Press, San Francisco, 239–246.

Bostick, B.C., Fendorf, S. (2003) Arsenite sorption on troilite (FeS) and pyrite (FeS_2). *Geochimica et Cosmochimica Acta* 67, 909–921. https://doi.org/10.1016/S0016-7037(02)01170-5

Butler, I.B., Schoonen, M.A.A., Rickard, D.T. (1994) Removal of dissolved oxygen from water: A comparison of four common techniques. *Talanta* 41, 211–215. https://doi.org/10.1016/0039-9140(94)80110-X

Donovan, J.J., Tingle, T.N. (1996) An Improved Mean Atomic Number Background Correction for Quantitative Microanalysis. *Microscopy and Microanalysis* 2, 1–7. https://doi.org/10.1017/S1431927696210013

Etschmann, B.E., Ryan, C.G., Brugger, J., Kirkham, R., Hough, R.M., Moorhead, G., Siddons, D.P., De Geronimo, G., Kuczewski, A., Dunn, P., Paterson, D., de Jonge, M.D., Howard, D.L., Davey, P., Jensen, M. (2010) Reduced As components in highly oxidized environments: Evidence from full spectral XANES imaging using the Maia massively parallel detector. *American Mineralogist* 95, 884–887. https://doi.org/10.2138/am.2010.3469

Etschmann, B.E., Donner, E., Brugger, J., Howard, D.L., de Jonge, M.D., Paterson, D., Naidu, R., Scheckel, K.G., Ryan, C.G., Lombi, E. (2014) Speciation mapping of environmental samples using XANES imaging. *Environmental Chemistry* 11, 341–350. https://doi.org/10.1071/EN13189

Howard, D.L., de Jonge, M.D., Afshar, N., Ryan, C.G., Kirkham, R., Reinhardt, J., Kewish, C.M., McKinlay, J., Walsh, A., Divitcos, J., Basten, N., Adamson, L., Fiala, T., Sammut, L., Paterson, D.J. (2020) The XFM beamline at the Australian Synchrotron. *Journal of Synchrotron Radiation* 27, 1447–1458. https://doi.org/10.1107/S1600577520010152

James-Smith, J., Cauzid, J., Testemale, D., Liu, W., Hazemann, J.-L., Proux, O., Etschmann, B., Philippot, P., Banks, D., Williams, P., Brugger, J. (2010) Arsenic speciation in fluid inclusions using micro-beam X-ray absorption spectroscopy. *American Mineralogist* 95, 921–932. https://doi.org/10.2138/am.2010.3411

Johnson, J.W., Oelkers, E.H., Helgeson, H.C. (1992) SUPCRT92: A software package for calculating the standard molal thermodynamic properties of minerals, gases, aqueous species, and reactions from 1 to 5000 bar and 0 to 1000°C. *Computers & Geosciences* 18, 899–947. https://doi.org/10.1016/0098-3004(92)90029-Q

Kusebauch, C., Oelze, M., Gleeson, S.A. (2018) Partitioning of arsenic between hydrothermal fluid and pyrite during experimental siderite replacement. *Chemical Geology* 500, 136–147. https://doi.org/10.1016/j.chemgeo.2018.09.027

Large, S.J.E., Bakker, E.Y.N., Weis, P., Wälle, M, Ressel, M., Heinrich, C.A. (2016) Trace elements in fluid inclusions of sediment-hosted gold deposits indicate a magmatic-hydrothermal origin of the Carlin ore trend. *Geology* 44, 1015–1018. https://doi.org/10.1130/G38351.1

Li, K., Etschmann, B., Rae, N., Reith, F., Ryan, C.G., Kirkham, R., Howard, D., Rosa, D.R.N., Zammit, C., Pring, A., Ngothai, Y., Hooker, A., Brugger, J. (2016) Ore Petrography Using Megapixel X-Ray Imaging: Rapid Insights into Element Distribution and Mobilization in Complex Pt and U-Ge-Cu Ores. *Economic Geology* 111, 487–501. https://doi.org/10.2113/econgeo.111.2.487

Qian, G., Brugger, J., Testemale, D., Skinner, W., Pring, A. (2013) Formation of As (II)-pyrite during experimental replacement of magnetite under hydrothermal conditions. *Geochimica et Cosmochimica Acta* 100, 1–10. https://doi.org/10.1016/j.gca.2012.09.034

Ram, R., Becker, M., Brugger, J., Etschmann, B., Burcher-Jones, C., Howard, D., Kooyman, P.J., Petersen, J. (2019) Characterisation of a rare earth element- and zirconium-bearing ion-adsorption clay deposit in Madagascar. *Chemical Geology* 522, 93–107. https://doi.org/10.1016/j.chemgeo.2019.05.011

Reich, M., Kesler, S.E., Utsunomiya, S., Palenik, C.S., Chryssoulis, S.L., Ewing, R.C. (2005) Solubility of gold in arsenian pyrite. *Geochimica et Cosmochimica Acta* 69, 2781–2796. https://doi.org/10.1016/j.gca.2005.01.011

Ryan, C.G. (2000) Quantitative trace element imaging using PIXE and the nuclear microprobe. *International Journal of Imaging Systems and Technology* 11, 219–230. https://doi.org/10.1002/ima.1007

Ryan, C.G., van Achterbergh, E., Jamieson, D.N., Churms, C.L. (1996) Overlap corrected on-line PIXE imaging using the proton microprobe. *Nuclear Instruments and Methods in Physics Research Section B: Beam Interactions with Materials and Atoms* 109–110, 154–160. https://doi.org/10.1016/0168-583X(95)00898-5

Ryan, C.G., Kirkham, R., Hough, R.M., Moorhead, G., Siddons, D.P., de Jonge, M.D., Paterson, D.J., De Geronimo, G., Howard, D.L., Cleverley, J.S. (2010) Elemental X-ray imaging using the Maia detector array: The benefits and challenges of large solid-angle. *Nuclear Instruments and Methods in Physics Research Section A: Accelerators, Spectrometers, Detectors and Associated Equipment* 619, 37–43. https://doi.org/10.1016/j.nima.2009.11.035

Ryan, C.G., Siddons, D.P., Kirkham, R., Li, Z.Y., de Jonge, M.D., Paterson, D.J., Kuczewski, A., Howard, D.L., Dunn, P.A., Falkenberg, G., Boesenberg, U., De Geronimo, G., Fisher, L.A., Halfpenny, A., Lintern, M.J., Lombi, E., Dyl, K.A., Jensen, M., Moorhead, G.F., Cleverley, J.S., Hough, R.M., Godel, B., Barnes, S.J., James, S.A., Spiers, K.M., Alfeld, M., Wellenreuther, G., Vukmanovic, Z., Borg, S. (2014) Maia X-ray fluorescence imaging: Capturing detail in complex natural samples. *Journal of Physics: Conference Series* 499, 012002. https://doi.org/10.1088/1742-6596/499/1/012002

Shock, E.L., Sassani, D.C., Willis, M., Sverjensky, D.A. (1997) Inorganic species in geologic fluids: Correlations among standard molal thermodynamic properties of aqueous ions and hydroxide complexes. *Geochimica et Cosmochimica Acta* 61, 907–950. https://doi.org/10.1016/S0016-7037(96)00339-0

Shvarov, Y.V. (1999) Algorithmization of the Numeric Equilibrium Modeling of Dynamic Geochemical Processes. *Geochemistry International* 37, 571–576.

Shvarov, Y., Bastrakov, E. (1999) *HCh: a software package for geochemical equilibrium modelling (v. 3.4).* User's Guide.

Smith, P.G., Koch, I., Gordon, R.A., Mondoli, D.F., Chapman, B.D., Reimer, K.J. (2005) X-ray Absorption Near-Edge Structure Analysis of Arsenic Species for Application to Biological Environmental Samples. *Environmental Science & Technology* 39, 248–254. https://doi.org/10.1021/es049358b

Sverjensky, D.A., Shock, E.L., Helgeson, H.C. (1997) Prediction of the thermodynamic properties of aqueous metal complexes to 1000°C and 5 kb. *Geochimica et Cosmochimica Acta* 61, 1359–1412. https://doi.org/10.1016/S0016-7037(97)00009-4

Su, W., Xia, B., Zhang, H., Zhang, X., Hu, R. (2008) Visible gold in arsenian pyrite at the Shuiyindong Carlin-type gold deposit, Guizhou, China: Implications for the environment and processes of ore formation. *Ore Geology Reviews* 33, 667–679. https://doi.org/10.1016/j.oregeorev.2007.10.002

Su, W., Heinrich C.A., Pettke, T., Zhang, X., Hu, R., Xia, B. (2009) Sediment-Hosted Gold Deposits in Guizhou, China: Products of Wall-Rock Sulfidation by Deep Crustal Fluids. *Economic Geology* 104, 73–93. https://doi.org/10.2113/gsecongeo.104.1.73

Su, W., Zhang, H., Hu, R., Ge, X., Xia, B., Chen, Y., Zhu, C. (2012) Mineralogy and geochemistry of gold-bearing arsenian pyrite from the Shuiyindong Carlin-type gold deposit, Guizhou, China: implications for gold depositional processes. *Mineralium Deposita* 47, 653–662. https://doi.org/10.1007/s00126-011-0328-9

Tanger, J.C., Helgeson, H.C. (1988) Calculation of the Thermodynamic and Transport Properties of Aqueous Species at High Pressures and Temperatures; Revised Equations of State for the Standard Partial Molal Properties of Ions and Electrolytes. *American Journal of Science* 288, 19–98. https://doi.org/10.2475/ajs.288.1.19

Wilkin, R.T., Barnes, H.L. (1996) Pyrite formation by reactions of iron monosulfides with dissolved inorganic and organic sulfur species. *Geochimica et Cosmochimica Acta* 60, 4167–4179. https://doi.org/10.1016/S0016-7037(97)81466-4

Xing, Y., Mei, Y., Etschmann, B., Liu, W., Brugger, J. (2018) Uranium Transport in F-Cl-Bearing Fluids and Hydrothermal Upgrading of U-Cu Ores in IOCG Deposits. *Geofluids* 2018, 6835346. https://doi.org/10.1155/2018/6835346

Xing, Y., Etschmann, B., Liu, W., Mei, Y., Shvarov, Y., Testemale, D., Tomkins, A., Brugger, J. (2019a) The role of fluorine in hydrothermal mobilization and transportation of Fe, U and REE and the formation of IOCG deposits. *Chemical Geology* 504, 158–176. https://doi.org/10.1016/j.chemgeo.2018.11.008

Xing, Y., Brugger, J., Tomkins, A., Shvarov, Y. (2019b) Arsenic evolution as a tool for understanding formation of pyritic gold ores. *Geology* 47, 335–338. https://doi.org/10.1130/G45708.1